Martin Cresnoverh, BSc

Realisation of a visual based condensation particle counter utilizing bright field technique

MASTER THESIS

For obtaining the academic degree
Diplom-Ingenieur

Master Programme of
Advanced Materials Science

Graz University of Technology

Supervisor:

Ao.Univ.-Prof. Dipl.-Ing. Dr.techn. Roland Resel

Institute of Solid State Physics

Graz, January 2015

EIDESSTATTLICHE ERKLÄRUNG

AFFIDAVIT

Ich erkläre an Eides statt, dass ich die vorliegende Arbeit selbstständig verfasst, andere als die angegebenen Quellen/Hilfsmittel nicht benutzt, und die den benutzten Quellen wörtlich und inhaltlich entnommenen Stellen als solche kenntlich gemacht habe. Das in TUGRAZonline hochgeladene Textdokument ist mit der vorliegenden Masterarbeit/Diplomarbeit/Dissertation identisch.

I declare that I have authored this thesis independently, that I have not used other than the declared sources/resources, and that I have explicitly indicated all material which has been quoted either literally or by content from the sources used. The text document uploaded to TUGRAZonline is identical to the present master's thesis/diploma thesis/doctoral dissertation.

_____ _____

Datum / Date Unterschrift / Signature

Acknowledgements

I would like to thank *Roland Resel* for his help and backing as my thesis supervisor at *TU Graz*.

At *AVL List* I would like to express my gratitude to my advisor and mentor *Alexander Bergmann*, who provided the initial idea for this thesis and supported and guided me through it. I also thank *Patrick Falk* for the good job creating his thesis; it was the base upon which this work was built.

My parents and grandparents I have to thank for providing me with an upbringing that made things like this possible.
And last, but not least, I would like to sincerely thank my fiancée *Beate* for always believing in me.

Abstract

Internal combustion engines produce a high number of aerosol nanoparticles. The measurement of the number concentration of these particles is typically performed with *Condensation Particle Counters*. In a previous work a method of optimizing the counting characteristics of such particle counters with a novel approach to the particle detection setup was designed and simulated. The present thesis focuses on the realization and characterization of a particle counting apparatus with the aforementioned optimized detection setup. It consists of a *Condensation Nucleus Magnifier*, which magnifies the nanoparticles to visually detectable sizes by condensing liquid (from a supersaturated gas atmosphere) on the particles; and an optical bright field detection unit, which uses a laser and a line scan camera for the detection of the particles. Comparisons with commercial Condensation Particle Counters revealed that the system was measuring particle number concentrations within the expected accuracy of $\pm 10\,\%$. Furthermore, the diameter of the particles magnified by the Condensation Nucleus Magnifier was determined with a custom built *Static Light Scattering* device to be at $(8.5 \pm 1.1)\mu m$. The findings of this work indicate a high potential for the usage of the new detection setup for Condensation Particle Counters in the future.

Kurzfassung

Verbrennungsmotoren erzeugen eine hohe Anzahlkonzentration an Aerosol-Nanopartikeln, welche üblicherweise mit *Kondensationspartikelzählern* gemessen wird. In einer früheren Arbeit wurde eine Methode zur Optimierung der Zählcharakteristik solcher Partikelzähler mittels eines neuen Detektionsaufbaus entwickelt und simuliert. Das vorliegende Werk beschäftigt sich mit der Realisierung und Charakterisierung einer Partikelzählapparatur mit dem zuvor erwähnten optimierten Detektionsaufbau. Diese Apparatur besteht zum einen aus einem *Kondensationskernvergrößerer*, der die Nanopartikel durch das Aufdampfen von Flüssigkeit (aus einer übersättigten Gasatmosphäre) auf optisch detektierbare Durchmesser vergrößert; zum anderen aus einer Hellfeld-Optikeinheit mit einem Laser und einer Zeilenkamera zur Detektion der Partikel. Der Vergleich mit kommerziell verfügbaren Kondensationspartikelzählern zeigte, dass eine Messung von Partikelanzahlkonzentrationen mit der erwarteten Genauigkeit von $\pm 10\,\%$ mit dem neuen System möglich ist. Zusätzlich wurde der Durchmesser der aus dem Kondensationskernvergrößerer austretenden Partikel mit einem speziell angefertigten Lichtstreusystem mittels *Statischer Lichtstreuung* zu $(8.5 \pm 1.1)\,\mu\text{m}$ bestimmt. Die Ergebnisse dieses Werkes lassen auf eine sehr gute Eignung des neuen Detektionsaufbaus für den Einsatz in Kondensationspartikelzählern schließen.

Contents

1. Introduction

1.1. Particle counting in automotive exhaust

The Particulate Mass (PM) emitted by modern motor vehicles that are powered by Diesel internal-combustion engines is very low due to the implementation of Diesel Particle Filters (DPFs) in the exhaust system. The classical method used for the determination of PM is the gravimetric analysis of filter samples: Via a heated hose the whole exhaust flow of the vehicle is brought to a Constant Volume Sampler (CVS) where it is diluted and cooled down to room temperature. This simulates some of the processes that happen when the exhaust is emitted into the atmosphere. The diluted exhaust is then passed through a measurement filter that collects the particulate matter. The mass of this filter is determined with a micro balance before and after loading it with particles, the difference being the mass of the deposited particles. This method is legislatively compulsory for the determination of vehicle emissions.

Since DPFs filter nearly all and especially larger (and heavier) particles, the sampled Particulate Mass is very small and can no longer be reliably measured.

Thus a new addition to the vehicle emissions legislation was introduced by the United Nations Economic Commission for Europe (UNECE) for the measurement of Particle Number (PN) in the Appendix 5 of Annex 4a of Regulation 83 (R83) [7]. This document defines a method for sampling emitted particles and measuring their number with a Particle Number Counter (PNC) as described in the next section.

1.1.1. Particle Sampling

Figure 1.1 shows a typical setup for the sampling of PN in compliance with R83 [14]. Primary particles are generated during the combustion of fuel inside the combustion chamber of the engine. These primary particles begin to form agglomerates immediately afterwards, while being transported through the exhaust line. Via a heated hose the whole exhaust flow is brought to a CVS tunnel. There, due to the cooling, gaseous components of the exhaust begin to condense; either by forming new nuclei or by condensing on already existing agglomerates. The newly condensed nuclei mainly consist of sulfuric acid (H_2SO_4), which origins e.g. from engine lubrication oil, or from unburnt fuel [15].

Some agglomerates are temporarily deposited along the flow path, form bigger particles (called *Coarse Mode*), and then rejoin the aerosol flow. This process is called reentrainment. These particles represent the main fraction of the PM, but since they are not as numerous as the small newly condensed *Nucleation Mode* particles, their contribution to PN is very minor. The left stylized graph of figure 1.2 shows the Number Concentration of the particles in the diluted exhaust depending on their size (=size distribution) inside of the CVS tunnel. As already explained, this size distribution consists of a *Nucleation Mode* with sizes of approximately 10 nm containing the highest number of particles, an *Accumulation Mode* mainly formed by the agglomerates with sizes of approximately 100 nm which is less numerous, and of the *Coarse Mode* with sizes in the order of 1000 nm with the least number of particles.

As shown on the right side of figure 1.1, this aerosol is then sampled out of the CVS tunnel into a hot dilution system. The dilution system consists of a hot dilution stage at 150 °C, a pipe with a wall temperature of 350 °C and a second cold dilution stage. The purpose of this system is to evaporate the volatile components of the sample (mainly the small sulfuric acid particles) and lower their partial pressures to prevent re-condensation. The total number of particles in the aerosol, which now has a size distribution as is shown in the right graph of figure 1.2, is then counted with a PNC.

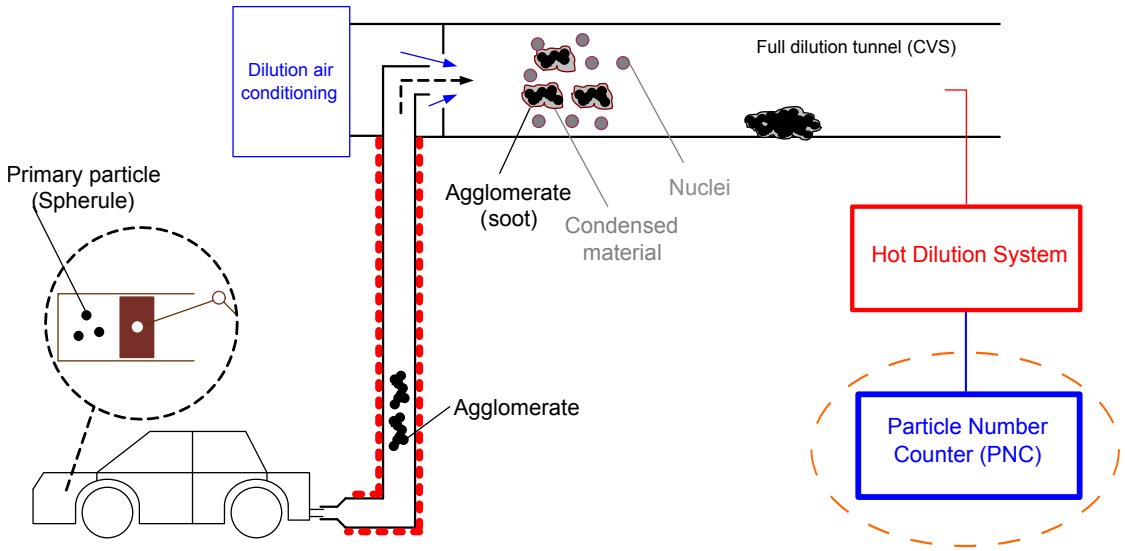

Figure 1.1.: Particle Number measurement of automotive exhaust [14].

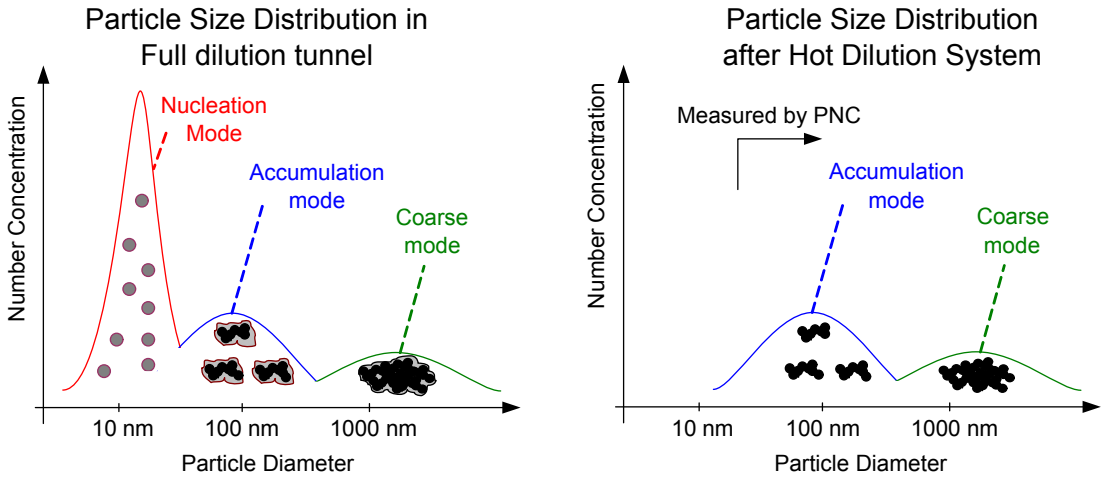

Figure 1.2.: Particle Size Distribution before and after the Hot Dilution System [14].

1.1.2. Particle Counting

The most typical particle counting method is to firstly force the aerosol (that contains the particles) through a nozzle, thus separating the particles in the flow direction. An area directly above the nozzle is illuminated by a light source. Particles that pass this area scatter the incident light, this scattered light is then measured by a photodiode, and finally the number of electrical pulses produced this way is counted.

If it is desired to count particles that are significantly smaller than the wavelength of the incident light (which is typically in the visible spectrum), the size of these particles has to be increased. This is done in Condensation Particle Counters (CPCs) by condensing a working fluid on the particles before counting them with the aforementioned principle. The growth stage is called Condensation Nucleus Magnifier (CNM) in this work.

1.2. Condensation Particle Counters

1.2.1. Components

As already explained, a CPC consists of two main parts: The growth stage, called CNM and the optical counting apparatus. A detailed description of CPCs can be found in chapter 19 of [1].

Figure 1.3 illustrates a typical setup for such a particle counter.

(1) Working fluid reservoir: Holds the working fluid (e.g. an alcohol or a hydrocarbon)
(2) Saturator: Temperature controlled block, contains the "wick" (a porous material) which transports the working fluid from the internal reservoir to the wall of the aerosol flow path where it is evaporated in order to mix with the aerosol flow. The saturator is kept at a temperature sufficient for evaporation of the working fluid.
(3) Condenser: Temperature controlled block containing the aerosol flow path upstream of the saturator with a wall temperature lower than the temperature of the saturator, this leads to supersaturation of the working fluid vapour present in the aerosol. The nanoparticles act as condensation

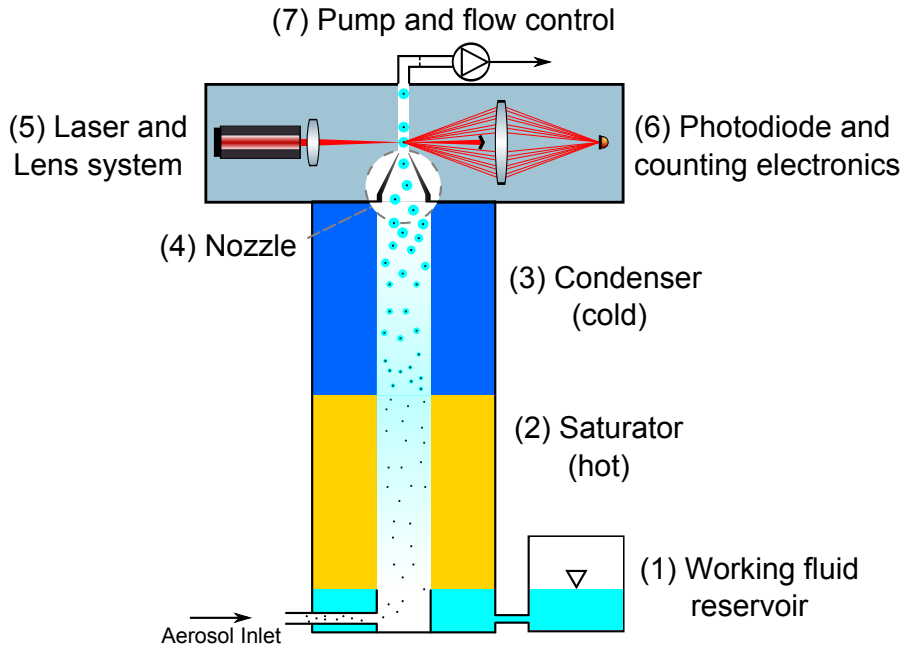

Figure 1.3.: Schematic of a Condensation Particle Counter (CPC).

nuclei for the supersaturated vapour and thus each of the nanoparticles becomes suspended in a droplet of the working fluid.

(4) Nozzle: The Nozzle focuses the aerosol stream that contains the "magnified" particles (=particles with condensed working fluid) to the illuminated area above. The particles are accelerated and thus separated spatially in the flow direction to lower the probability for coincidence events (in a coincidence event two particles are in the same plane normal to the flow direction and can thus not be counted separately).

(5) Laser and Lens system: They are used to create an illuminated plane above the nozzle through which the particles pass. Then, the laser beam is terminated at a beam stop. The light scattered by the particles in the illuminated area can bypass the beamstop and is focused by a convex lens onto the photodiode (This type of optical setup is called "Dark field").

(6) Photodiode and counting electronics: The intensity of the scattered light that is focused on the photodiode has to be measured with high time resolution because the light pulses are relatively short due to the speed of the particles when exiting the nozzle. The counting electronics count the number of pulses; then the particle number concentration can be calculated if the flow through the CPC is known.

(7) Pump and flow control: The flow through the device is provided by a pump at the end of the aerosol flow path. The flow rate is typically defined by a critical orifice which provides a constant volume flow rate if the vacuum downstream of the orifice is sufficiently low.

1.2.2. Counting characteristics

The supersaturated working fluid only forms droplets around particles that are bigger than the so called *Kelvin Diameter* d_p. The minimum saturation ratio S_R that is necessary to start the condensation process on a particle with a diameter d_p is described by the Kelvin equation (Chapter 5 of [1]):

$$S_R = \exp\left(\frac{4 \cdot \gamma \cdot M}{\rho_P \cdot R \cdot T \cdot d_P}\right) \tag{1.1}$$

S_R... Saturation ratio (ratio of the partial pressure of the vapor to the saturation vapor pressure)
γ... Surface tension of the working fluid
M... Molecular weight of the working fluid
ρ_P... Density of the working fluid in liquid state
R... Gas constant
T... Temperature
d_P... Kelvin diameter

Thus, if the saturation ratio that is kept at a certain value, condensation will always start at a certain particle diameter. In a real CPC, the saturation ratio will always vary minimally in the condenser, because of (1.1) this causes a certain variation of the Kelvin diameter.

Typically, the detection efficiency of a CPC is shown in a "counting efficiency curve" as displayed in figure 1.4, which plots the fraction of detected particles as a function of the particle size. The particle diameter, at which only 50 % of the present particles are still counted, is called D_{50} or cut-off size. This particle diameter can be adjusted by changing the temperature difference between the saturator and condenser, which changes the saturation ratio of the working fluid vapor in the condenser [4].

CPCs that are used for measurements within R83 are required to have a cut-off-size of 23 nm (Section 1.3.4.8 of Appendix 5 of [7]). Usually, it is easily possible

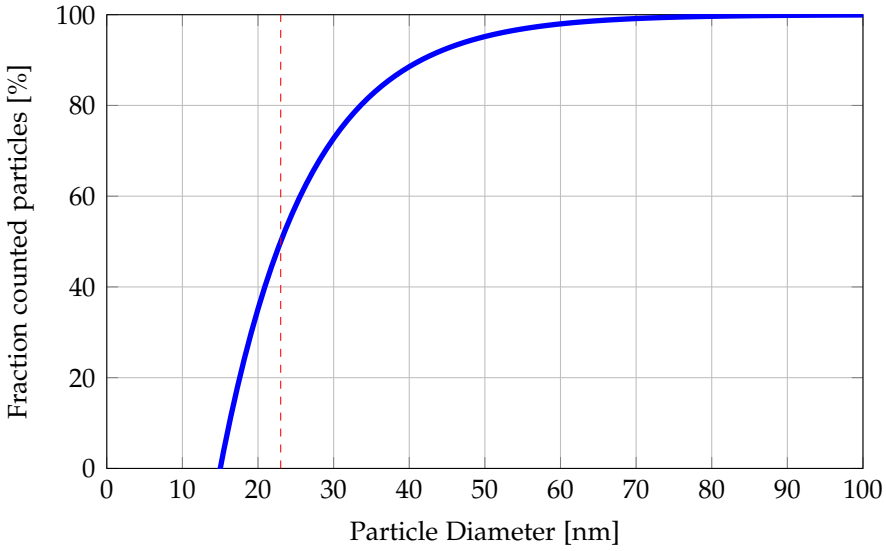

Figure 1.4.: Typical CPC counting efficiency curve. The red dashed line shows the cut-off-size of $D_{50} = 23\,\text{nm}$. Modeled as described appendix A of [25].

to archive a cut-off-size of about 5 nm; however, the legislators decided to use the higher cut-off-size of 23 nm as a second safeguard to avoid measuring the small nucleation mode particles (as explained in section 1.1.1).

1.3. Optimization of particle number counting

Optical detection setups containing a nozzle and a single photodiode as described in section 1.2 have a high probability for coincidence events when measuring high particle number concentrations. Coincidence events occur when two particles are in the same plane normal to the flow direction and can thus not be counted separately.

A correction for these coincidence events can be applied, as is for example described in [20]. The legislation for particle number measurements only allows for a coincidence correction of up to 10 % of the measured concentration (Section 1.3.4.7 of Appendix 5 of [7]). The maximum concentration that can typically be measured by a CPC before reaching this coincidence limit is in the range of $10\,000\,\text{cm}^{-3}$ to $20\,000\,\text{cm}^{-3}$. This is mainly due to hardware limitations, namely that the velocity of the particles cannot be increased indefinitely. Also,

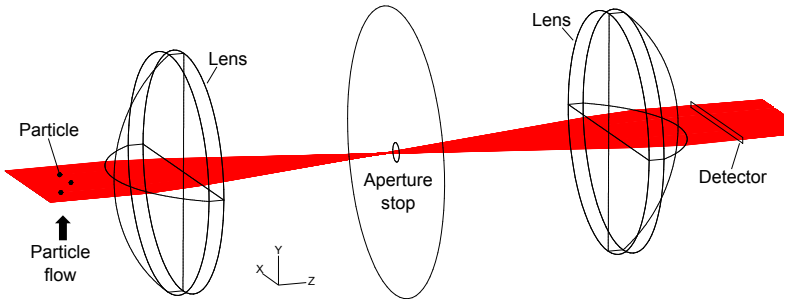

Figure 1.5.: Bright field setup as suggested in [8].

the counting of extremely short pulses that result from these high velocities is only possible down to a certain minimal pulse length.

In [8] different methods to reach lower coincidence probabilities were theoretically discussed and simulated. The most promising setup evaluated in this work is shown in figure 1.5.

The main features of this new setup are:

1. Bright field instead of dark field.
2. No nozzle.
3. Array photo sensor instead of a single photodiode.

The main intention of this setup is to lower the coincidence probability by simultaneous detection of a number of particles at the same time.

As is shown in figure 1.5, a flat laser beam passes, starting from the left side, through the particle flow, wherein a portion of the light is scattered by the particles. The rest of the laser beam passes through a convex lens, an aperture stop, and again a convex lens. This kind of setup is called a double telecentric lens, it's purpose in this assembly is mainly to block the light scattered by the particles within the detection plane. Finally, the laser beam reaches the detector, which is a line photo array.

The shadow of a passing particle will now be visible as a decrease in illumination intensity on the detector and should thus be easily detectable.

This setup, further on called "scatter-abatement optics" was already briefly tested in [8] with 20 µm Polystyrene Latex (PSL) Particles (no CNM was used). The results of this experiment indicate that it should be possible to detect particles, however only a single particle was identified with certainty.

2. Experimental evaluation of the scatter-abatement optics

A more thorough experimental evaluation of the bright field setup invented in [8] and explained in section 1.3 was performed to clarify whether usage in a CPC is possible.

For this purpose a CNM and a flow control unit were built and attached to the scatter-abatement optics.

2.1. Experimental setup

2.1.1. Condensation Nucleus Magnifier

The operating principle of the CNM is basically described by items (1) to (3) in section 1.2; in the following paragraph the implementation of the described elements will be explained briefly (figure 2.1).

(1) Working fluid reservoir: The liquid level is controlled by a capacitive level sensor and a solenoid valve which controls the supply from an external working fluid tank (not displayed). The working fluid used is n-Decane ($C_{10}H_{22}$).
(2) Saturator: The temperature control circuit consists of a PT100 temperature sensor and a thermoelectric heat pump. The temperature of the saturator is kept at 38 °C; the control circuit controls the temperature within less than ±0.1 °C.
(3) Condenser: The temperature is controlled with a system similar to the one in the saturator; the temperature is typically kept at 29 °C.

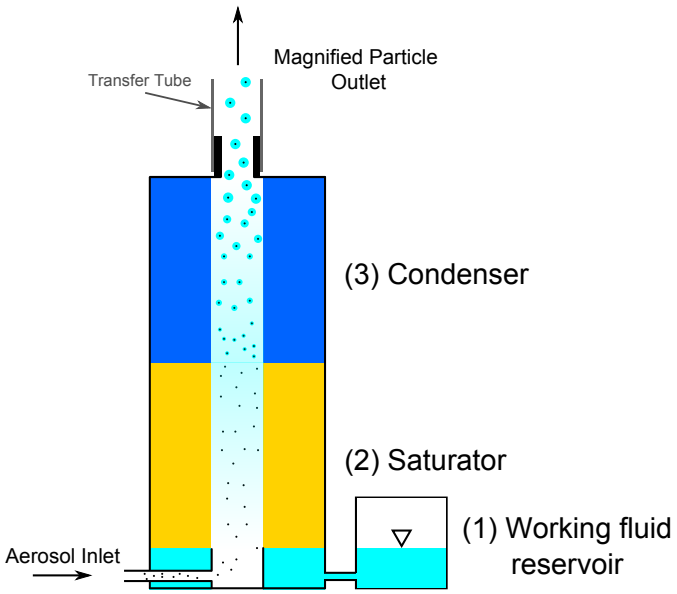

Figure 2.1.: Schematic of the CNM.

(4) Magnified particle outlet: The inner diameter of the condenser outlet is 5 mm, on top of the outlet a transfer tube with an inner diameter of 7.8 mm and a length of about 20 mm is mounted.

Since it was only intended to test the functionality of the new optical detection setup, the cut-off size of the CNM was not determined precisely. However, prior measurements with similar setups have shown that with a saturator temperature of 38 °C and a condenser temperature of 29 °C the cut-off-size is typically in the range of $\sim$ 20 nm.

The diameter of the particles leaving the CNM was estimated to (7 ± 2) µm by computer simulations prior to this work.

It can be assumed that the shape of the particles is spherical because they are basically liquid droplets that only have a very small condensation nucleus in the center, in a relatively slow air flow.

2.1.2. Aerosol source

Since the main target of these experiments was to establish a proof that the bright field setup works in general, no rigorous requirements were claimed

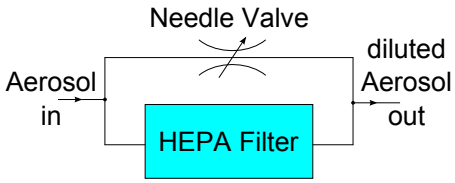

Figure 2.2.: Dilution bridge for particle concentration control.

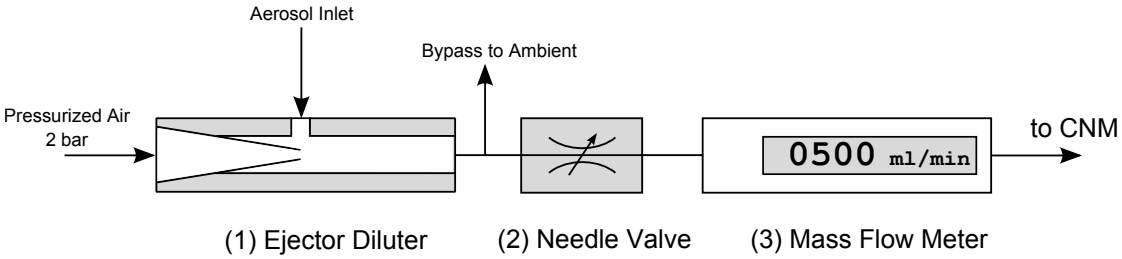

Figure 2.3.: Gas flow path of the flow control unit.

for the aerosol source. The particle number concentration of the room air that was measured in the laboratory with a commercial CPC (with a cut-off-size of 23 nm), was in the range of 1000 to 10 000 cm^{-3}. Typically, the majority of these particles is in the size range of 50 to 500 nm [9].

Thus the ambient air in the laboratory is sufficient as a particle source. In order to be able to measure particle concentrations lower than that of the ambient air, a "dilution bridge" is used. This widget consists of a High Efficiency Particulate Air (HEPA)-Filter and a needle valve, these components are connected as is shown in figure 2.2.

If the needle valve is completely closed, the aerosol is forced through the HEPA-Filter, where all particles are removed. Thus only particle free air will exit the dilution bridge. If the needle valve is completely opened, the aerosol will pass almost exclusively through the valve because the HEPA-Filter has a higher pressure drop. Thus nearly undiluted aerosol will exit the dilution bridge. By adjusting the needle valve, the dilution can now be regulated between these extremes.

2.1.3. Flow Control

The aerosol flow needs to be provided upstream of the saturator, because the particles are emitted to ambient air at the particle outlet of the CNM (=downstream of the condenser). As is shown in figure 2.3, this is done with an ejector diluter (1) that samples and dilutes the ambient air using the venturi principle. The sampled and diluted air is then provided with overpressure to a bypass and to a needle valve (2). The needle valve regulates the flow into the CNM, this flow is then measured with a thermal Mass Flow Meter (MFM) (3) (Model *TSI* 4143 [24]).

This flow meter shows the volumetric flow rate q_{MFM} (with a precision of $\pm 2\,\%$) at preset standard conditions ($T_{std} = 21.11\,°C$, $p_{std} = 1013\,\text{mbar}$). In order to calculate the volumetric flow rate q_{arb} at arbitrary temperature and pressure conditions (T_{arb}, p_{arb}), one can use the ideal gas law in good approximation (chapter 13 of [29]):

$$\frac{p \cdot V}{T} = m \cdot R_s \tag{2.1}$$

p... Pressure in gas volume [mbar]
V... Considered volume [cm^3]
T... Gas temperature [K]
m... Mass of gas in volume [kg]
R_s... Specific gas constant [J/kgK]

V can be substituted with the volumetric flow rate q_V; $(m \cdot R_s)$ is always the same for one mass flow rate. Thus the volumetric flow at arbitrary conditions can be calculated by:

$$q_{arb} = q_{MFM} \cdot \frac{p_{std}}{p_{arb}} \cdot \frac{T_{arb}}{T_{std}} \tag{2.2}$$

For typical ambient conditions in the laboratory ($p_{arb} = 970\,\text{mbar}$, $T_{arb} = 25\,°C$) the normalization factor is approximately 1.06; this factor was *not* taken into account unless otherwise stated.

The volumetric flow rate was usually set to a value between $300\,\text{cm}^3\,\text{s}^{-1}$ and $1000\,\text{cm}^3\,\text{s}^{-1}$, depending on the experimental necessities.

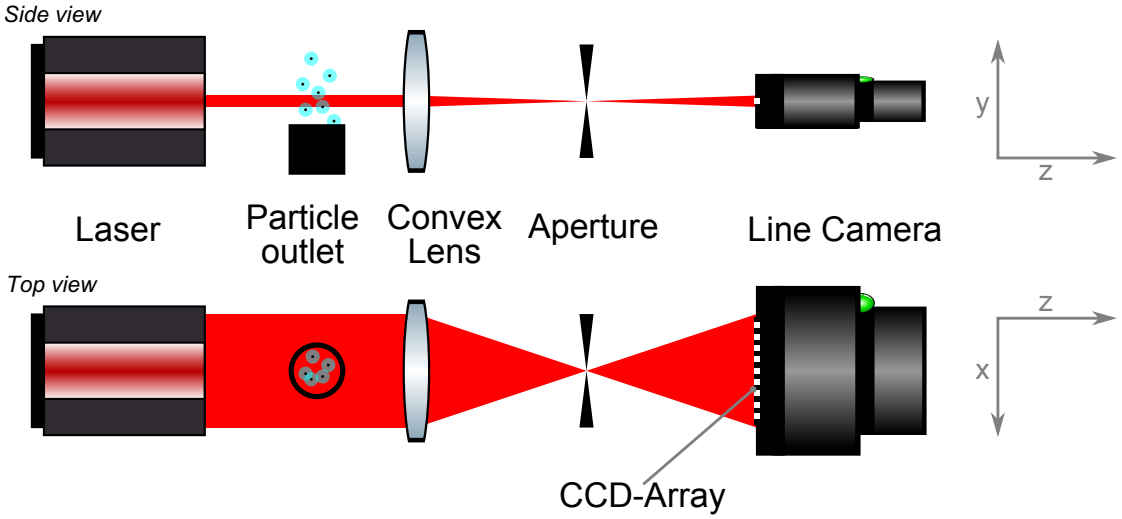

Figure 2.4.: Schematic of the scatter-abatement optics.

2.1.4. Scatter-abatement optics

The initial bright field detector setup, called scatter-abatement optics (figure 2.4), which is derived from the setup shown in figure 1.5, consists of four main elements: A collimated laser, a convex lens, an aperture and a line camera.

The following components were used:

Laser: Low Noise Coherence (LNC) laser module by *Schäfter+Kirchhoff* with the following specifications [16]:

Identifier: LNC-91CM-M60-635-1-H02-H-6
Wavelength: 635 nm
Power: 1 mW
Beam profile: approximate rectangle of 14 × 3 mm
Beam divergence: 0.03 mrad
Laser Class: 2
Adjustable output power: 1 to 100 %

Lens: Plan-convex lens by *Qioptiq* with the following specifications:

Identifier: G063103322
Focal length: 80 mm
Diameter: 31.5 mm

Aperture: Iris aperture by *Qioptiq* with the following specifications:

Identifier: G050533000
Aperture diameter: adjustable, 0.5 – 7 mm

Line camera: Monochrome line scan camera by *Schäfter+Kirchhoff* with the following specifications [17]:

Identifier: SK1024U3PD
Sensor type: *DALSA* IL-P1-1024
Number of Pixels: 1024
Pixel size: 10 µm × 10 µm
Maximum line frequency: 43.478 kHz
Exposure time: 0.01 ms to 20 ms
Spectral range: 400 nm to 1000 nm

The maximum line frequency of 43.478 kHz means that the minimum exposure time that can be chosen for a continuous acquisition of scan lines is $(43.478 \times 10^3)^{-1} = 0.023$ ms. Exposure times shorter than this lead to "dead time" in which no data acquisition takes place.

Operating principle of the scatter-abatement optics

As already mentioned, the scatter-abatement optics (figure 2.4) are similar to the setup shown in figure 1.5, except that the second condenser lens of the aperture stop is omitted. This was done in order to be able to magnify the incident laser beam on the line camera with a simple movement of the camera along the beam axis (z).

The collimated beam of the laser passes over the particle outlet, where particles cause diffraction, refraction and absorption. The beam is then focused with the plan-convex lens and passes through the aperture which is mounted in the focal point of the lens ($f = 80$ mm). The aperture keeps out diffracted light that is no

longer propagating in a similar direction as the incident laser beam. Then the beam reaches the detector where a decrease in the intensity of the incident light can be determined and localized because of the aforementioned interaction of the particles with the light. The size of the incident beam can be varied by movement of the line camera along the optical axis. Distances from aperture to the end of the sensor plane of the camera of 125 mm to 270 mm were used (resulting in a magnification of 1.6× to 3.4×).

2.1.5. Reference Condensation Particle Counter measurements

For some measurements an external reference CPC was used to verify that the visualized particles correlate with the particle number concentration of the aerosol. The device utilized for this measurements was a commercial CPC from *TSI*. The inlet of the CPC was connected with a T-Piece to the "Bypass to Ambient" as is shown in figure 2.5.

Specifications of the CPC [23]:

Manufacturer: *TSI Inc.*
Identifier: 3790 Engine Exhaust CPC
Serial Number: 3790112302
Cut-off size: $D_{50} = 23\,\text{nm}$
Concentration accuracy: $\pm 10\,\%$ compared to standard

2.1.6. Complete Setup

The schematic of the complete setup, containing the aforementioned components for flow control and dilution, the CNM, the bright field detection unit, and the reference CPC can be seen in figure 2.5. Figure 2.6 shows a picture of the setup during measurement (only a part of the flow control section is visible).

2.1.7. Data acquisition and processing

The line camera is equipped with an USB 3.0 interface for the transfer of the image data to a computer. The manufacturer provides *Microsoft Windows* device

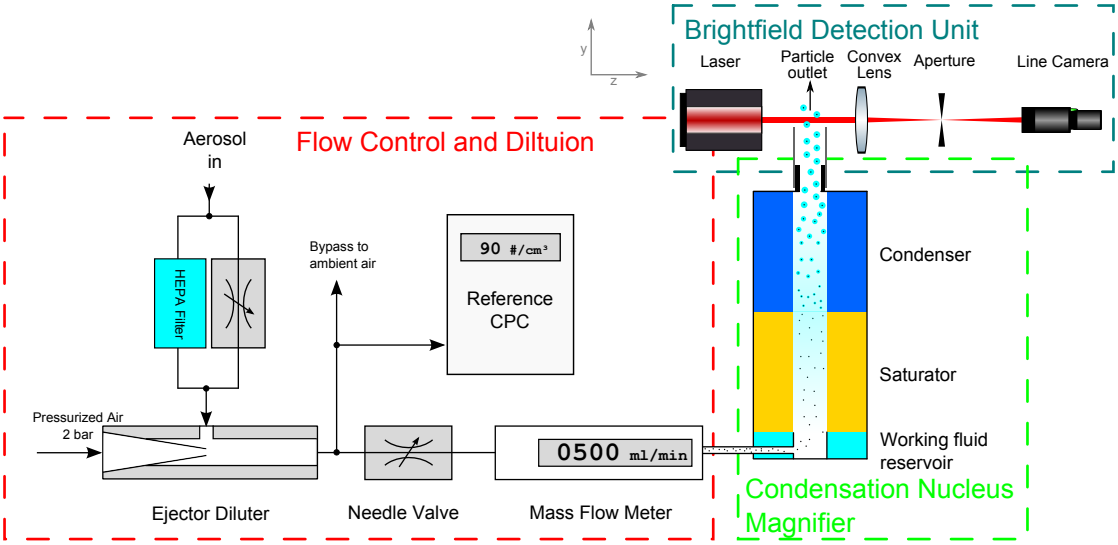

Figure 2.5.: Schematic of the complete measurement setup.

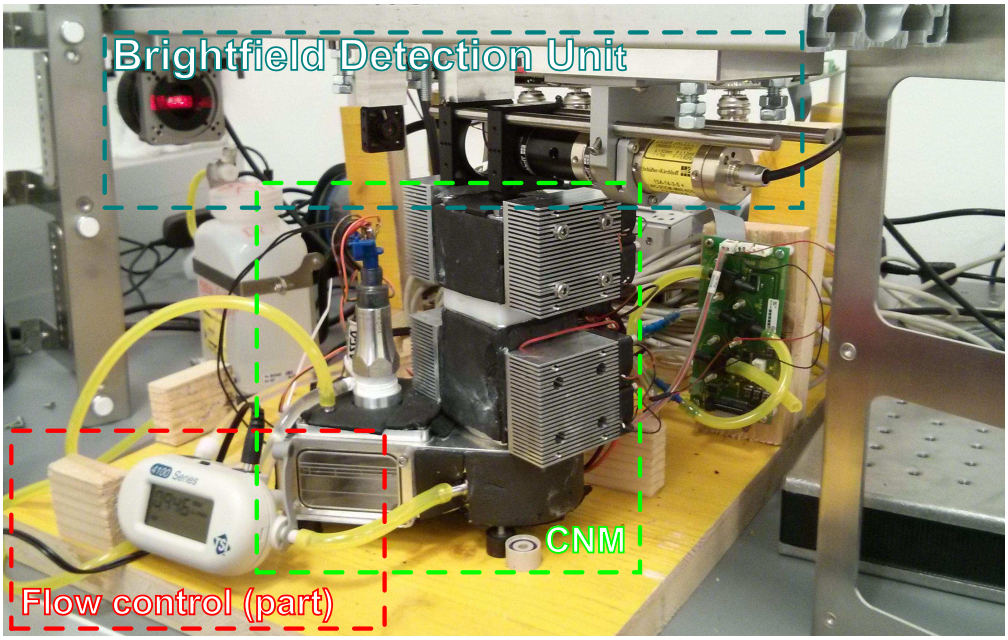

Figure 2.6.: The whole setup with the scatter-abatement optics during measurement.

drivers and a C++ library for easy access to the functions of the camera. This library was used to write a simple command line program in *Microsoft Visual C++* called *cam_usb* (source code in appendix C.1). This program takes the exposure time per line, and the number of lines to record as command line parameters and outputs a comma-separated-value file (CSV-file) with the sensor data at a 12bit resolution.

For convenient data processing *GNU Octave* (A *Matlab*® compatible Open Source programming language [31]) was used. The program *cam_usb* was called from within *Octave* to acquire the raw data of the line sensor, further data manipulation and plotting was then done with *Octave*.

2.2. Experiments with the scatter-abatement optics

For the first experiment a distance between sensor plane and aperture of 270 mm was chosen in order to magnify the particle shades with an expected diameter of 7 µm (section 2.1.1) by a factor of approximately 3.4×. The aperture was closed to the minimum diameter of 0.5 mm to keep out as much light as possible scattered by the particles.

2.2.1. Determination of the exposure time

The exposure time was estimated with the following assumptions:

1. The aerosol flow exiting the transfer tube at the highest used flow rate (section 2.1.3) still has a laminar flow profile. This can be assumed because of the low *flow Reynolds number*; Re $<$ 2000 means laminar flow (chapter 4 of [1]).

$$\mathrm{Re} = \frac{4 \cdot \rho \cdot q}{\eta \cdot d \cdot \pi} = 158 \tag{2.3}$$

Re...Reynolds number
ρ...Air density (=1.161 kg m^{-3}) (for 300 K, page 6-1 of [28])
q...Volumetric air flow (=1000 cm^3 min^{-1}=16.67 $\times$ 10^{-6} m^3 s^{-1})
η...Air viscosity (=1.86 $\times$ 10^{-5} Pa s) (for 300 K, page 6-201 of [28])
d...Tube diameter (=7.8 $\times$ 10^{-3} m)

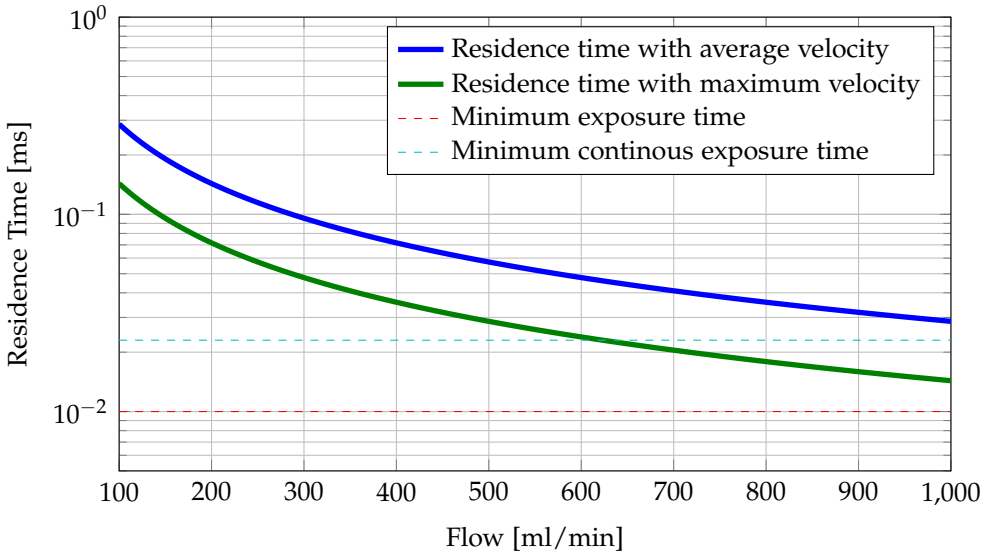

Figure 2.7.: Calculated residence time of a particle in a length of 10 µm (=Sensor height) dependent on the laminar flow the particle is in for an outlet diameter of 7.8 mm.

2. Because of their relatively small size, the particles follow the gas flow velocity profile very closely (chapter 4 of [1]). Thus it can be assumed that the particle velocity is equal to the gas velocity.

3. The height of the sensor pixel line is $h_{sen} = 10\,\mu m$.

4. The average gas velocity in a laminar flow v_{av} can be calculated out of the volumetric flow rate q_v with (chapter 4 of [36]):

$$v_{av} = \frac{4 \cdot q_v}{d^2 \cdot \pi} \tag{2.4}$$

5. The maximum velocity v_{max} can then be simply calculated with:

$$v_{max} = 2 \cdot v_{av} \tag{2.5}$$

6. The residence time of a particle with velocity v in the sensor area is:

$$t_{res} = \frac{h_{sen}}{v} \tag{2.6}$$

Figure 2.7 shows the residence time of a particle in front of the line sensor as a function of the flow rate using equations (2.4) to (2.6).

It was decided that for the intended flows of approximately $300\,\mathrm{cm^3\,s^{-1}}$ to $1000\,\mathrm{cm^3\,s^{-1}}$ an exposure time in the range of 0.023 ms to 0.035 ms should generally be sufficient.

2.2.2. Data processing

The sensor data was usually recorded as a continuous series of 1000 lines (unless otherwise stated) with an exposure time per line in the range stated in section 2.2.1. Figure 2.8 shows the average intensity for each pixel for an arbitrary measurement (The ordinate goes up to $2^{12} = 4096$, this is the intensity where the sensor reaches saturation.). The average measured intensity is approximately 40 % of the saturation intensity.

Figure 2.9 shows the measured sensor data as a 1024×1000 pixel grayscale image, with the abscissa representing the spatial dimension (x-axis) and the ordinate representing the time dimension. Because of the spatial intensity fluctuation of the laser it is necessary to subtract a background value for each pixel. Since the aim of the measurements was to find particles that have a residence time in front of the line sensor, that is in the order of magnitude of the exposure time per line, it can be assumed that the intensity value of one pixel will change when a particle passes during the recording of 1000 lines. Thus the averaged intensity value for each pixel over the 1000 lines, as already displayed in figure 2.8, was subtracted from each recorded line. Using this very procedure, figure 2.10 and all other similar images were produced.

The dynamic range of the background corrected image is 56 steps in the case of figure 2.10 (compared to the sensor bit depth of 12bit = 4096 steps). Also later images never exceeded a range of 200 steps of the initial bit depth. Thus it was decided that the background corrected images could be safely stored as 8-bit pictures ($2^8 = 256$ steps) without any loss of information. This means also that for further processing of the images less memory and processor time is necessary.

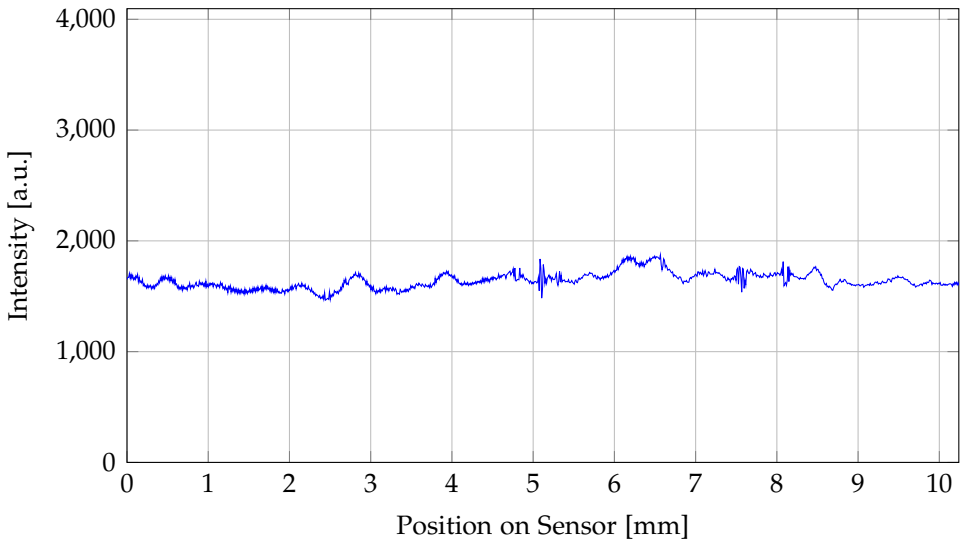

Figure 2.8.: Measured sensor intensity with 0.035 ms exposure time per line on the scatter-abatement optics, averaged over 1000 lines. The limits of ordinate are the full intensity scale of the camera.

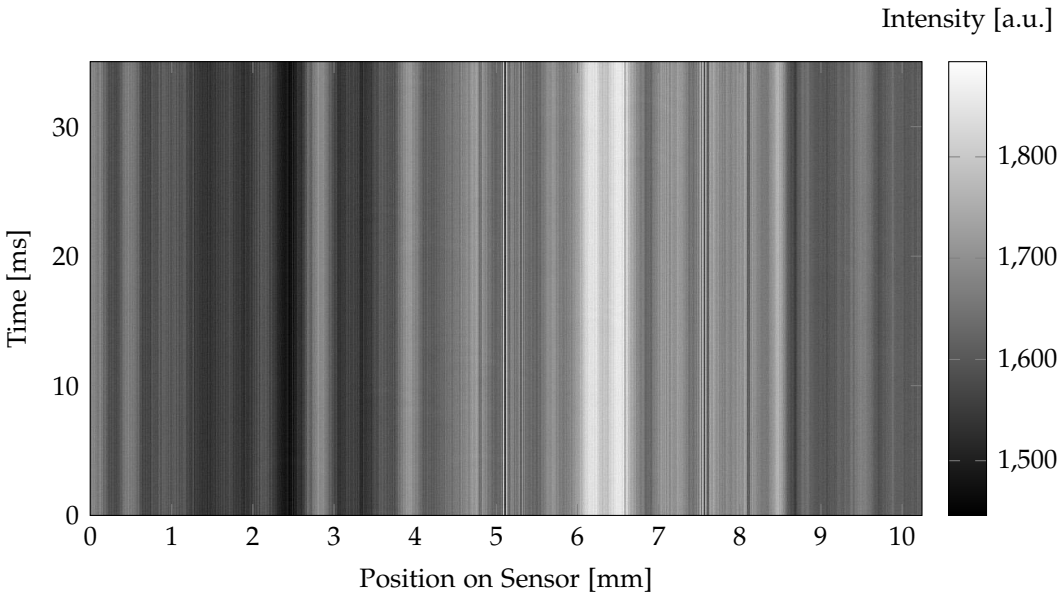

Figure 2.9.: Absolute intensity recorded with the scatter-abatement optics.

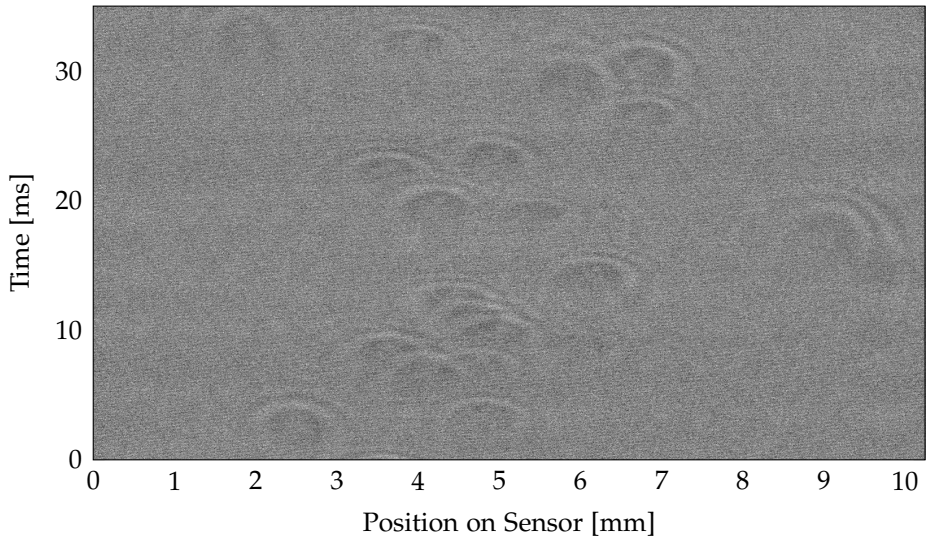

Figure 2.10.: Background corrected intensity, recorded with th scatter-abatement optics. The aerosol flow was set to 380 $cm^3\,min^{-1}$, the exposure time per line to 0.035 ms. 19 particles are visible.

2.2.3. Comparison of measured number concentrations with the reference

Figure 2.10 obviously shows elliptical patterns that are visible above the noise. The intensity of these features is relatively low. The patterns overlay at some parts, but it is possible to distinguish between the separate patterns nevertheless. These patterns are created by the particles passing through the detection plane.

The ambient air that was supplied during the acquisition of the image was diluted with the dilution bridge as described in section 2.1.2.

In order to get the confirmation that these patterns are indeed produced by single particles originating from the CNM, an external reference CPC was connected to the setup as described in section 2.1.5. This CPC measured a concentration of $C_{CPC} = (90 \pm 10)\,cm^{-3}$ during the image acquisition period.

The flow passing the sensor was measured with the MFM at $q_{MFM} = 380\,cm^3\,min^{-1}$ ($\widehat{=}$ $6.33\,cm^3/s$), the exposure time per line was set to $t_S = 0.035\,ms$, and $n_L = 1000$ lines were recorded.

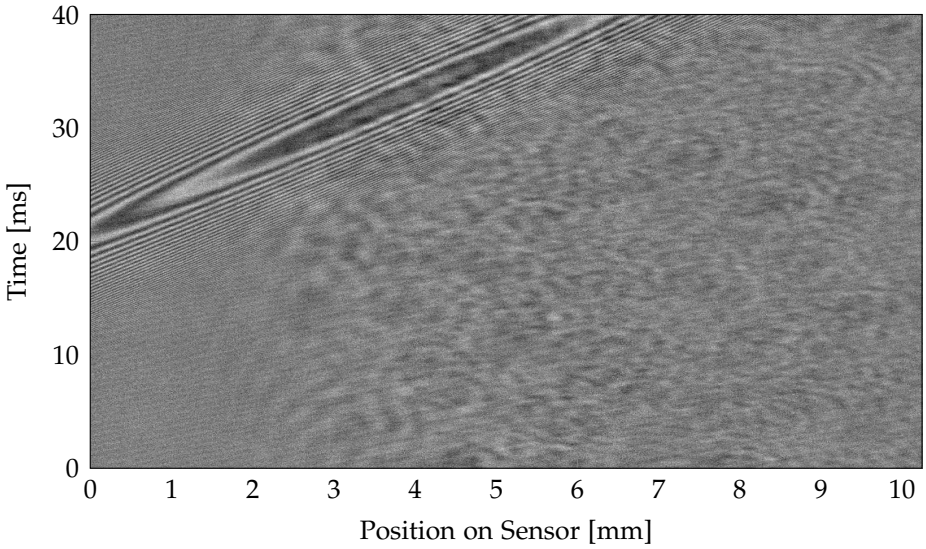

Figure 2.11.: Background corrected intensity, recorded with the scatter-abatement optics. At higher concentrations particles are no longer easily distinguishable. Large ambient dust particles are an additional problem.

The particle number concentration can now be calculated by dividing the number of particles that are visible in the recorded image with the volume that passed through the detection plane during the time the image was recorded:

$$C_{calc} = \frac{n_P}{q_{MFM} \cdot n_L \cdot t_S} \tag{2.7}$$

In figure 2.10, $n_P = 19$ different elliptical patterns can be distinguished; assuming that this is the number of particles, with equation (2.7) this corresponds to a particle number concentration of $C_{calc} = 85.8\,\mathrm{cm}^{-3}$. This correlates very nicely to the concentration measured with the reference CPC ($C_{CPC} = (90 \pm 10)\,\mathrm{cm}^{-3}$).

Appendix B.1 contains further images recorded in this measurement series; the calculated and measured concentrations are noted in the image captions.

2.2.4. Measurement of higher concentrations

Figure 2.11 shows the background corrected intensity when providing ambient particles without dilution (the concentration is estimated to be at $1000\,\mathrm{cm}^{-3}$

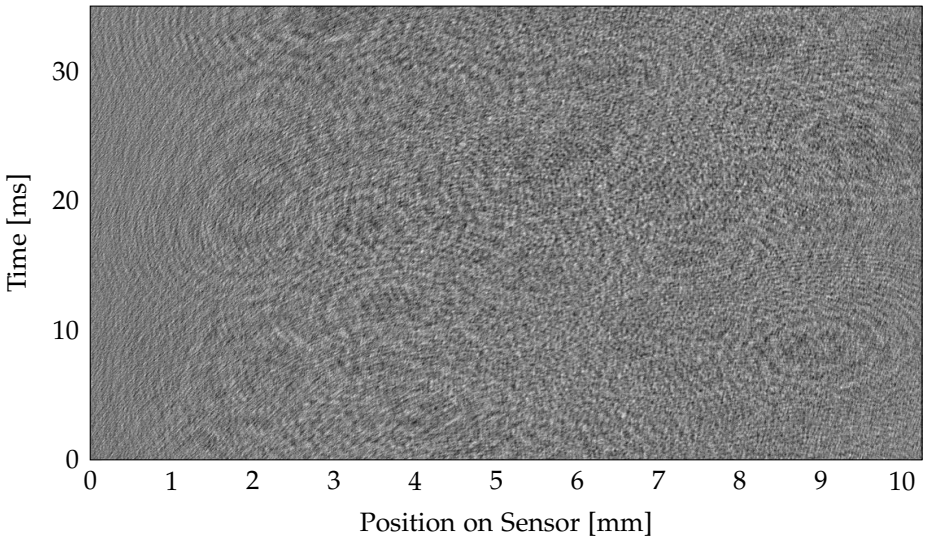

Figure 2.12.: Background corrected intensity, recorded with the scatter-abatement optics. With fully opened aperture, a high number of rings appears.

to 2000 cm^{-3}). The particles are no longer distinguishable, thus the scatter-abatement optics are not easily suitable for the counting of higher particle concentrations.

Additionally, a large elliptical pattern is visible in the upper left side of the figure. It has to be assumed that this is a "big" (probably $> 10\,\mu m$) ambient dust particle passing the optical path between line camera and aperture (figure 2.4), otherwise the light scattered by the particle would be blocked by the aperture. Events like these were observed relatively often (approximately one in five recorded images); they can happen because the optical path was neither enclosed nor sealed against ambient air. For figure 2.12 the aperture was completely opened and undiluted ambient air was measured. A high number of rings appears around the particles, making it even more difficult to distinguish between different particles.

3. Experimental evaluation of the direct-beam optics

Since the scatter-abatement optics had not been not adequate for counting particles at higher particle number concentrations, it was decided to simplify the setup and examine whether this new setup had better performance characteristics.

3.1. Experimental Setup

Figure 3.1 shows the schematic of the simplified optics, further on called "direct-beam optics". The lens and aperture were omitted, instead the line camera was moved more closely to the particle outlet. The other parts like flow control and CNM were left as described in section 2.1.

The distance in the laser beam direction (z-axis) between the center of the particle outlet and the plane of the line sensor was approximately 23 mm.

3.2. Experiments

Figure 3.2 shows an image of 1000 lines with an exposure time per line of 0.023 ms and a flow of 860 $cm^3\,min^{-1}$ at ambient concentration. The average measured intensity with this setup and exposure time was 64 % of the saturation intensity. Single particles are relatively easy to distinguish after subtracting the average intensity for each pixel as described in section 2.2.2. The number of particles was estimated to $\sim$ 320 by manually counting the particles in one

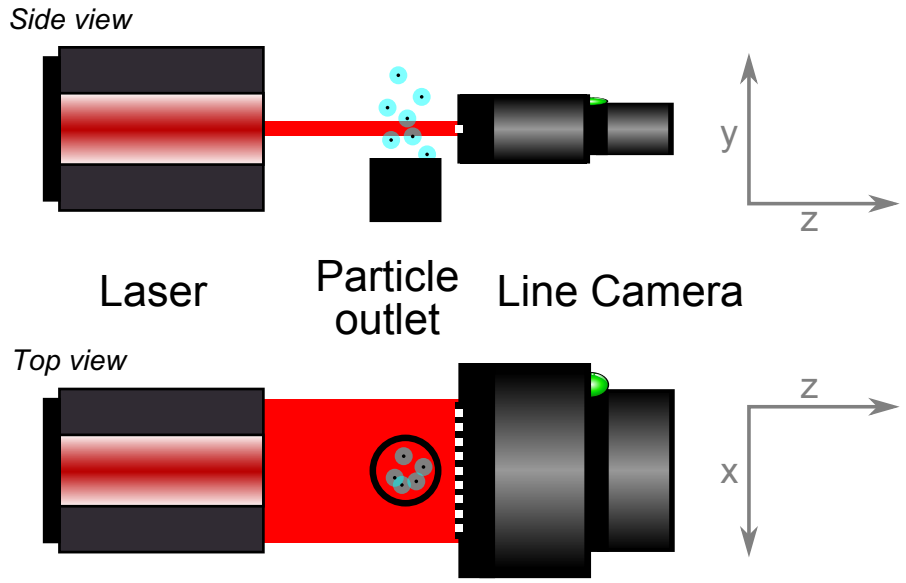

Figure 3.1.: Schematic of the direct-beam optics.

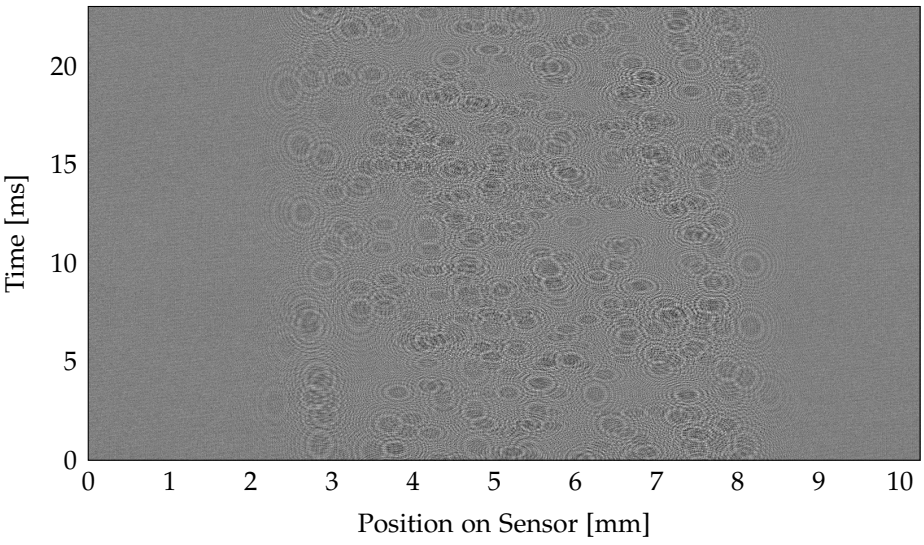

Figure 3.2.: Measurement with the direct-beam optics. The aerosol flow was set to 860 $cm^3\,min^{-1}$, the exposure time per line to 0.023 ms, 1000 lines were recorded.

tenth of the image. The particle number concentration calculated with (2.7) thus is approximately $1000\,\mathrm{cm}^{-3}$.

A closer look at figure 3.2 reveals that around each particle there is a huge number of rings. The relative intensity of these rings does not decrease very much from the inside to the outside, thus diffraction can be ruled out as a main origin of these patterns. However, since the light emitted by the laser is coherent, it can be assumed that *interference* is causing the formation of the patterns.

The means of producing interference patterns of an object within the light path of coherent light on an image plane is called *In-Line Holography*.

3.3. In-Line Holography

In-Line holography was the first kind of holography invented; it was developed by Dennis Gabor in 1948 [13]. Initially, the intention was to improve the resolution of electron microscopes. However, it was quickly realized that holography can be used for any coherent electromagnetic wave and can thus be useful in many applications.

The basic principle of In-Line Holography can be seen in figure 3.3. It can be broken down into the following simple steps:

1. Illumination of a sensor (camera) with a coherent plane wave from a laser (=*reference wave*).
2. Small objects within the illuminated area act as scattering centers (=*object wave*).
3. Interference of the reference and the object wave forms an interference pattern at the image plane.

The great advantage of holography in general is the possibility to store three-dimensional information in a two-dimensional image. The coherent electromagnetic waves that caused the interference pattern can be reconstructed because the pattern contains information about amplitude and phase of these waves (chapter 9 of [18]). The process of extracting the information about the incident waves and rebuilding them is known as *Hologram Reconstruction*.

Typical photosensitive materials (analog or digital) can only store intensity information directly. The phase information of the object wave is encoded in the

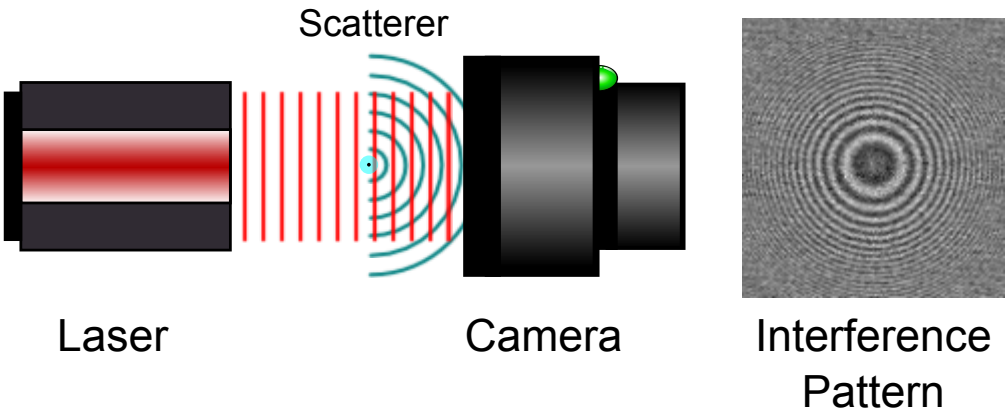

Figure 3.3.: General principle of In-Line Holography.

interference pattern and can be extracted because the properties of the reference wave are exactly known.

Analog holography uses photographic film or plate for the recording of the interference pattern, the reconstruction can be achieved by illumination of the recorded image (that is transparent at the areas where no intensity was recorded) with the reference wave. This leads to diffraction of the reference wave at the interference pattern and reconstructs the light field of the object in the same way as it was recorded.

Nowadays digital photo sensors and digital data processing have become very easily available, thus the numerical reconstruction of light fields has become the standard in most holographic applications. One numerical method used for reconstruction will be discussed in section 3.3.2. The process of producing In-line holograms and recording and reconstructing them digitally has become known as *Digital In-Line Holography (DIH)*.

3.3.1. Applications of Digital In-Line Holography

Recently, DIH has been used in different disciplines extensively. The following section only mentions a few research papers relying on this method. Soft Matter Physics/Colloidal Physics:

- The method is used for the determination of the Boltzmann's constant with very high precision [27].
- The measurement of translational, rotational, and vibrational dynamics in colloids with DIH is described in [12].

Aerosol Physics:

- The technique is used for in situ detection of atmospheric cloud particles [10].
- A system three-dimensionally imaging single aerosol particles in flight is described [2].

Biology:

- Imaging of living testate amoeba is performed [5].
- Digital holography is used for the depiction of living cells and microbes [30].

The simplicity of the setup needed for DIH (basically only a simple laser and an image sensor are necessary) enables the building of holography imaging systems with off-the-shelf components. In [35] a consumer scanner is used to record high-resolution gigapixel holograms.

3.3.2. Angular Spectrum Method for the reconstruction of holograms

Several methods are available for the reconstruction of holograms. This section only focuses on the method used for this work, the Angular Spectrum Method (ASM).

The scalar diffraction theory can be formulated in a way that closely resembles the theory of linear, invariant systems. This so called ASM offers a relatively simple way for reconstructing holograms and has been implemented in software libraries for hologram reconstruction (e.g. *CWO++* [34]). The predictions for

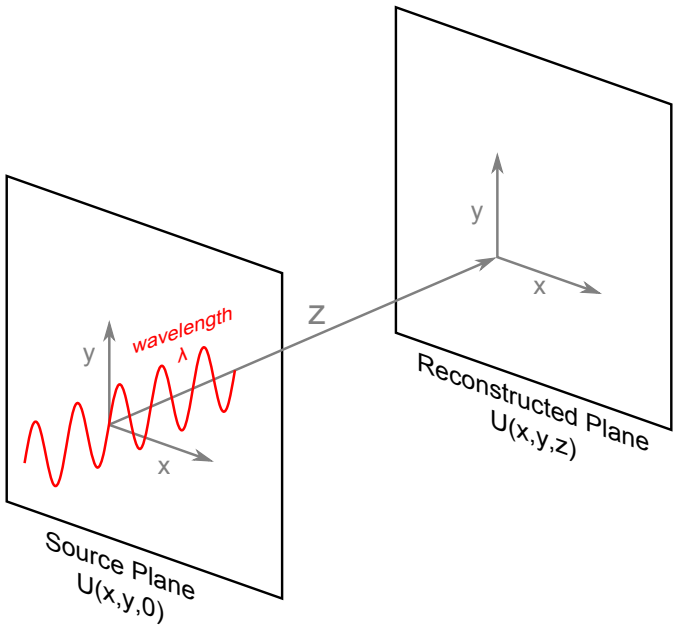

Figure 3.4.: Calculation from a source plane (=recorded hologram) to a reconstructed plane with ASM.

diffracted fields made with the angular spectrum method are identical to those made with the first Rayleigh-Sommerfeld solution (chapter 3 of [18]).

The ASM can be used to calculate the propagation of waves emitted by a monochromatic source. The field $U(x,y,z)$ (figure 3.4) of an electromagnetic plane wave can thus be reconstructed along the z-Axis, if the optical field is known at a plane $z = 0$:

$$U(x,y,z) = \iint_{-\infty}^{+\infty} A(f_x,f_y,0) \cdot H_A(f_x,f_y,z) \cdot \exp(2\pi i(f_x x + f_y y))\mathrm{d}f_x\mathrm{d}f_y \quad (3.1)$$

f_x, f_y...Fourier transformed coordinates

$A(f_x,f_y,0)$ is the two dimensional Fourier transformation of the plane at $z = 0$, $U(x,y,0)$:

$$A(f_x,f_y,0) = \iint_{-\infty}^{+\infty} U(x,y,0) \cdot \exp(-2\pi i(f_x x + f_y y))\mathrm{d}x\mathrm{d}y \quad (3.2)$$

H_A is the transfer function of the angular spectrum and is described as:

$$H_A(f_x, f_y, z) = \exp\left(2\pi i \frac{z}{\lambda}\sqrt{1-(\lambda f_x)^2-(\lambda f_y)^2}\right) \tag{3.3}$$

λ...Wavelength of the incident light

This transfer function is only valid within a certain range, namely:

$$\sqrt{f_x^2+f_y^2} < \frac{1}{\lambda} \tag{3.4}$$

If the frequencies are discretized with Δf_x and Δf_y as sampling pitches ($f_x = m\Delta f_x$, $f_y = n\Delta f_y$), and the Fourier transformation is replaced with a Fast Fourier Transformation (FFT), the whole process of the ASM can be written as:

$$U(m,n,z) = \text{IFFT}\left[\text{FFT}(U(m,n,0)) \cdot H_A(m,n,z)\right] \quad , \tag{3.5}$$

where IFFT is the inverse FFT.

The discretized ASM is one of the reconstruction methods available in *CWO++*.

3.3.3. Numerical Hologram Reconstruction with CWO++

CWO++ [34] is an open source Computational Wave Optics library for C++. It implements different hologram reconstruction algorithms and offers the possibility to parallelize the calculation on multiple processor cores or even on *NVIDIA* Graphics Processing Units (GPUs).

With this library a C++ command line program called *cwo_reconstruct* (source code in appendix C.2) was written in *Microsoft Visual C++* that takes the path to a interference pattern image as input parameter and then calculates n reconstructions with the ASM evenly spaced in a distance d_{min} to d_{max} from the sensor plane. The properties of the holographic setup (Wavelength of the laser $\lambda = 635\,\text{nm}$ and sensor pitch $\Delta x = 10\,\mu\text{m}$) are hard coded into the source code. The format of the input image file has to be either BMP, JPEG, PNG, or TIFF. The reconstructed intensity images are output into the same path and with the same format as the input image. Each reconstruction is a separate image, the intensity of the images is always scaled to occupy the full dynamic range

that is available for the bit depth of the output format. This means that the intensity of similar areas in different reconstruction distances can vary because the maximum and minimum intensities to which the image intensity is scaled can be different for these various reconstruction planes.

The GPU implementation could not be used because the computer utilized for the calculations did not possess a *NVIDIA* graphics card. However, calculation of the reconstructions was still relatively fast on the CPU, partly because of the low bit-depth of the recorded interference pattern images of 8 bit (section 2.2.2), and partly because parallelization could be used on the quad-core *Intel* Core i7-4800MQ CPU with 2.7 GHz and Hyperthreading. The calculation of one reconstruction with the ASM at a resolution of 1024×1000 pixels took about 0.8 s.

3.4. Exemplary reconstruction of a single particle

For the purpose of reconstructing a single particle with *cwo_reconstruct*, a holographic image was taken at a very low concentration (figure 3.5, 1000 lines, exposure time per line 0.023 ms, flow 470 $\mathrm{cm}^3\,\mathrm{min}^{-1}$). The particle marked with the yellow rectangle was cropped out for further processing. The cropped image's distortion was manually corrected in the time axis to resemble a perfectly circular pattern. This is necessary because it is assumed for the ASM that the hologram is recorded with a two-dimensional sensor. Thus only the shape of the particles defines the form of the interference pattern. With a line sensor (as used here) this is not the case, as the form of the interference patterns is defined not only by the shape but also by the velocity of the particles. Since it can be assumed that the particles are spheres (section 2.1.1), the correction of the shape in the time axis to the known geometry is allowed.

Figure 3.6 shows the particle with applied distortion correction. The picture was sheared until the main axis of the elliptic interference pattern was perfectly normal to the sensor axis. Then the time axis was scaled until a perfectly round shape was archived. Thus now the pattern should look very similar to a pattern recorded with a two-dimensional sensor. The image was not manipulated in the sensor axis, so the size of the sensor pixels still defines the physical sizes of the pixels in the image. Also note that the dimension of the ordinate was changed from time to space for the corrected image.

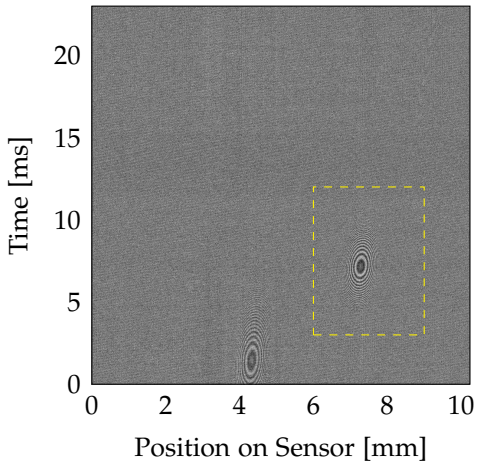

Figure 3.5.: Image taken at very low concentration. The particle in the yellow rectangle was selected for the reconstruction.

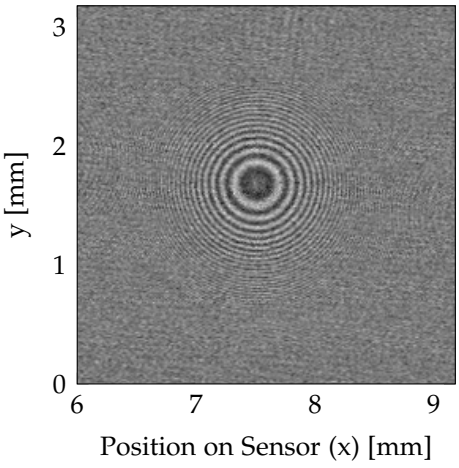

Figure 3.6.: Single particle with applied distortion correction in the former time-axis. The ordinate dimension was changed to space.

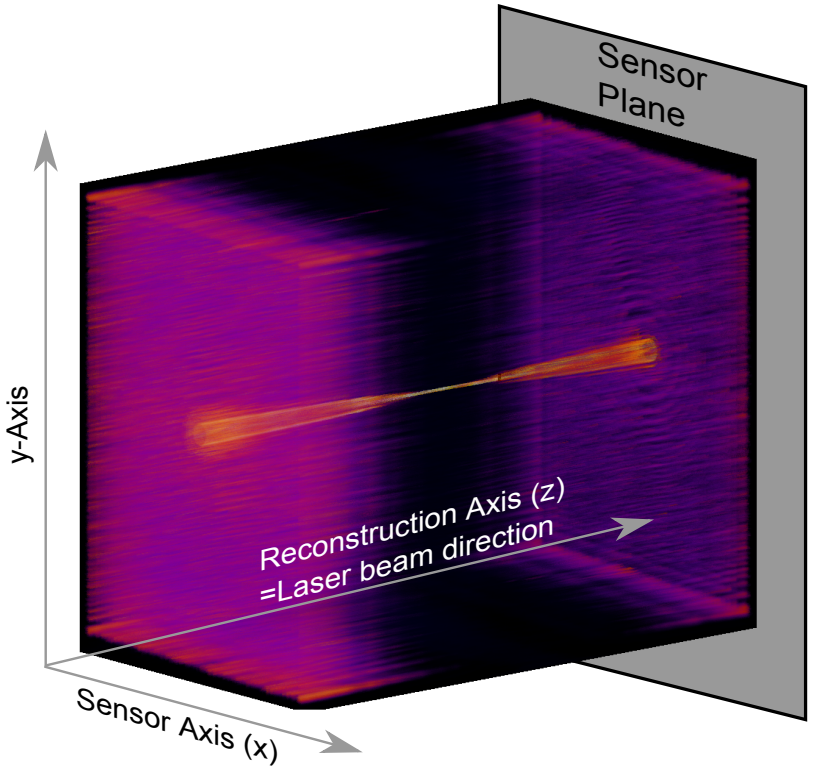

Figure 3.7.: Volume reconstruction of the single particle.

Furthermore, this image was then processed with *cwo_reconstruct* to produce a reconstruction of the light field with 200 reconstructed images starting at a distance from the sensor (i.e. the z-axis) of 16 mm up to 28 mm. Figure 3.7 shows a volume representation of the 200 reconstructed images stacked together. This image was produced with the Volume Viewer of *ImageJ* [33], an open source scientific image processing program.

It is clearly visible that the spatial extension of the maximum intensities (orange) of the x-y-planes has a minimum approximately in the middle of the reconstruction axis. This is the position of the particle in the laser beam direction (z-axis). It is also visible is that at the beginning and at the end of the volume in the reconstruction axis there are additional intensities (colored purple). This is due to the problem of scaling each reconstruction image to its optimal contrast as has been mentioned in section 3.3.3.

Appendix B.2 contains further images that were recorded with the direct-beam optics and hologram reconstructions of these images.

3.4.1. Particle Size estimation

Figure 3.8 shows a cross-section parallel to the sensor plane (x-y) through the volume displayed in figure 3.7. Its position is 22.7 mm before the sensor plane. Figure 3.9 shows a cross-section normal to the sensor plane (y-z), 7.5 mm in the sensor plane. The yellow line in figure 3.9 marks the position of the cross-section displayed in figure 3.8. This is the position of the particle in the reconstruction axis because of the minimal extension of the intensity in the y-direction.

The round yellow circle in figure 3.8 displays a 15× magnified view of the particle which reveals that only one pixel of the image is still completely occupied by the particle. This means, that the size of the particle has to be very close to, or even smaller than the pixel size of 10 µm.

This is already in good compliance with the sizes of (7 ± 2) µm mentioned for the particles exiting the CNM in section 2.1.1. However, the size cannot be determined precisely with the current holography setup. For a higher resolution of the imaged particles a smaller pixel pitch of the line camera would be necessary. A more precise determination of the particle size was done in chapter 4.

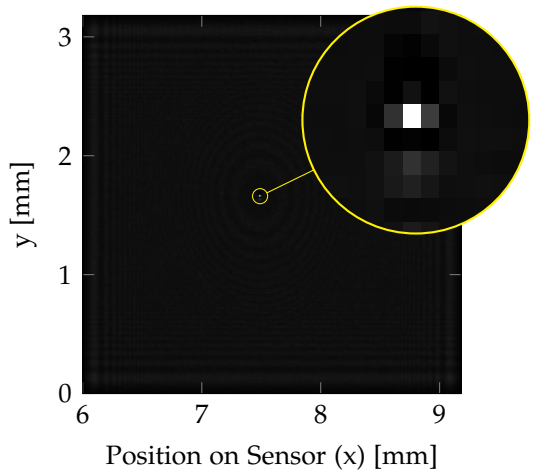

Figure 3.8.: Reconstruction 22.7 mm before sensor plane.

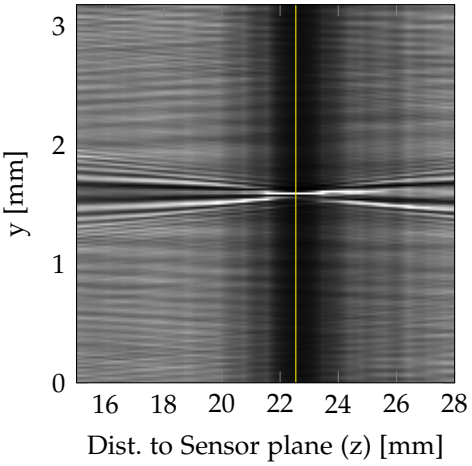

Figure 3.9.: Cross section at 7.5 mm in sensor plane.

3.5. Particle velocity determination

In section 2.1.1 it was mentioned that the particles leaving the CNM are nearly perfect spheres because they are basically only liquid droplets with a small particle in the middle. This property can now be taken advantage of for the determination of the velocities of these very particles.

Since the images taken with the line camera always have one space dimension and one time dimension, the information about the movement of the particles during the time the image was recorded line for line, has to be present in the picture.

3.5.1. Formalism for the velocity determination

With the following assumptions and constraints the particle velocity can be determined:

1. The recorded images have quadratic pixels.

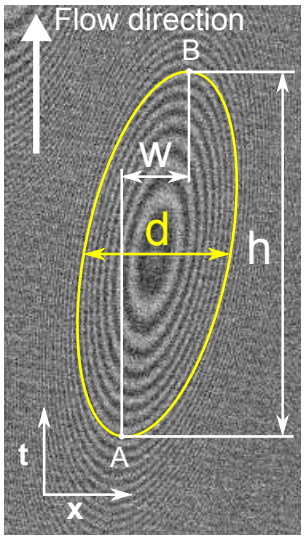

Figure 3.10.: Apparent diameter d, distance w, and height h.

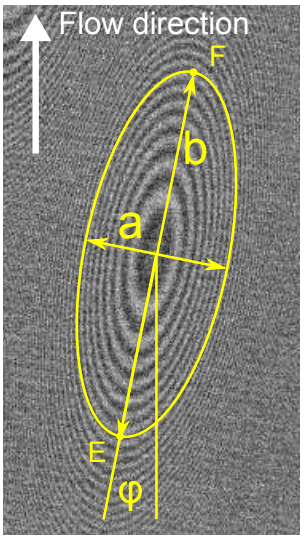

Figure 3.11.: Fitted ellipse with main axes a and b, and tilting angle φ.

2. The nomenclature of the axes is as follows (depiction of the position of the axes in figure 3.1):
   t-axis: time dimension (ordinate of the image)
   x-axis: line sensor direction (abscissa of the image)
   y-axis: aerosol flow direction
   z-axis: laser beam direction/reconstruction axis
3. The physical scale in the x-direction is defined by the pixel pitch of the of the line sensor to $\Delta x = 10\,\mu m$.
4. In t-direction it is known that from line to line the exposure time per line t_{exp} has passed.
5. The interference patterns of the particles that appear on the pictures are elliptic, they have an apparent height h in t-direction and an apparent center diameter d in x-direction (figure 3.10). Additionally, there is a distance w between the points A and B in x-direction that is > 0 if the main axis b of the ellipse (shown in figure 3.11) is not parallel to the t-axis. Do note that the points A and B on figure 3.10 differ from the points E and F on figure 3.11. The unit of all aforementioned distances is pixels.
6. The movement of the particles is in positive y-direction (they pass from below to above the detection plane).
7. The velocity vector of the particles does not change during the time the interference pattern is recorded.

A perfectly round interference pattern ($h = d$, $w = 0$) of a sphere would now mean that the distance s_{par} traveled by the particle with velocity v_y, is equal to the physical width of the interference pattern d_p.

$$s_{par} = t_{exp} \cdot h \cdot v_y, \quad d_p = d \cdot \Delta x \tag{3.6}$$

Thus the velocity in y-direction can be expressed as:

$$v_y = \frac{d}{h} \cdot \frac{\Delta x}{t_{exp}} \tag{3.7}$$

If the interference pattern is sheared ($w \neq 0$), there is also a velocity component in x-direction. It can then be calculated by:

$$v_x = \frac{w}{h} \cdot \frac{\Delta x}{t_{exp}} \tag{3.8}$$

Theoretically, it should also be possible to use the volume reconstructions of the light field to extract information about the velocity in the z-direction. However, in this case the velocity vector would have to be derived e.g. from the deviation of the reconstructed ellipsoid from a sphere. This means that the form of the particle has to be reconstructed with sufficient resolution, and currently, this is not the case (section 3.4). Additionally, as described in chapter 1.3 of [11], the resolution of the reconstruction axis is usually not as high as the sensor resolution.

In vector notation the projection of the velocity vector onto the sensor plane can thus be written as:

$$\vec{v}_{xy} = \frac{1}{h} \cdot \begin{pmatrix} d \\ w \end{pmatrix} \cdot \frac{\Delta x}{t_{exp}} \tag{3.9}$$

The absolute value of the velocity vector in the sensor plane can then be obtained out of:

$$v_{xy} = \frac{1}{h} \cdot \sqrt{d^2 + w^2} \cdot \frac{\Delta x}{t_{exp}} \tag{3.10}$$

Calculation of apparent height and diameter

If ellipses are fitted to the interference patterns with a computer program (e.g. *ImageJ*), the parameters given for these ellipses are most likely the sizes of the main axes a and b as well as the tilting angle φ, as is shown in figure 3.11. The equations (3.7) to (3.10) however require the apparent height h, the apparent diameter d and the distance w. These values can be calculated with the following formalism. It is assumed that b always is the axis with a tilting angle of less than 45° to the vertical (opposed to common notation where b usually is the smaller main axis).

The equation for a rotated ellipse is:

$$\frac{(x\cos\varphi - y\sin\varphi)^2}{a^2} + \frac{(x\sin\varphi + y\cos\varphi)^2}{b^2} = 1 \tag{3.11}$$

This equation can be derived in x as is shown in [26].

$$\frac{\mathrm{d}y}{\mathrm{d}x} = -\frac{a^2x\sin^2\varphi + y(a-b)(a+b)\sin\varphi\cos\varphi + b^2x\cos^2\varphi}{a^2y\cos^2\varphi + x(a-b)(a+b)\sin\varphi\cos\varphi + b^2y\sin^2\varphi} \tag{3.12}$$

This equation can now be equated to zero and after some conversions the apparent height h can be calculated out of a,b, and φ with the following equation:

$$h = \sqrt{(a\sin\varphi)^2 + (b\cos\varphi)^2} \tag{3.13}$$

The parameter w can also be calculated by equating (3.12) to zero and substituting h:

$$w = \frac{-h(a-b)(a+b)\cos\varphi\sin\varphi}{(a\sin\varphi)^2 + (b\cos\varphi)^2} \tag{3.14}$$

The apparent diameter d can be calculated with the polar form of the ellipse equation:

$$d = \frac{a\cdot b}{\sqrt{(a\sin\varphi)^2 + (b\cos\varphi)^2}} \tag{3.15}$$

3.6. Exemplary velocity and position determination

An arbitrary interference image with a relatively low particle concentration (diluted ambient air) was selected for the exemplary manual extraction of particle velocities and positions. Additionally this information was used to fit a laminar flow profile to the velocities.

3.6.1. Velocity determination

Figure 3.12 shows the interference image, recorded over 1000 lines with t_S=0.023 ms exposure per line. 27 ellipses were "manually" fitted with *ImageJ* to the sufficiently visible particles ("Manually" means that the outline of each ellipse was drawn by hand first, this line was then fitted by *ImageJ*). With the measured flow of $q_{MFM} = 595\,\mathrm{cm^3\,min^{-1}}$ the concentration calculated with (2.7) was $118\,\mathrm{cm^{-3}}$.

In table 3.1 the parameters of the fitted ellipses are listed. Additionally the apparent height and diameter as well as the distance w were calculated with (3.13) to (3.15) and the velocities were then determined with (3.9) and (3.10). Figure 3.13 shows the calculated velocity vectors on top of the interference image. A minor tendency of the direction of the vectors toward the left side is visible. The reason for that is an imperfection of the experimental setup, namely that the outlet pipe was not aligned perfectly normal to the line sensor axis.

3.6.2. Position determination

In order to obtain the particle positions in the z-axis, the command line program *cwo_reconstruct* (section 3.3.3) was used to create 1000 reconstructed images, starting at a distance of 15 mm up to 35 mm from the sensor. Opposite to the reconstruction described in section 3.4, no distortion correction had been applied to the image before the reconstructions were calculated since this is only possible for one particle at a time.

Figure 3.14 shows such an image, reconstructed 20.1 mm before the sensor plane. Since the recorded hologram is no "classical" two-dimensional interference image (because one axis is always the time-axis), the reconstruction of the distorted interference rings does not shrink them to a minimal area as has been

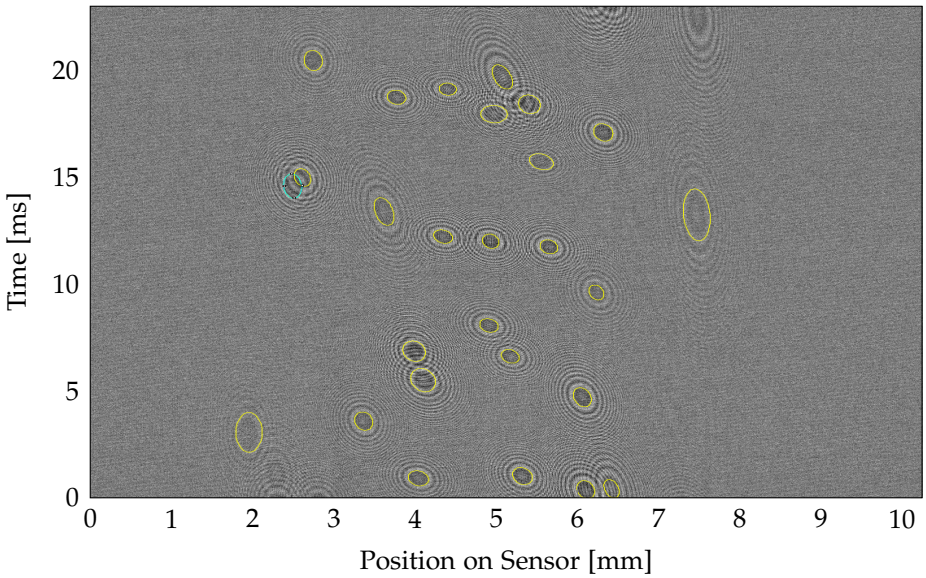

Figure 3.12.: Interference patterns recorded over 1000 lines with 0.023 ms exposure per line. The flow was set to 595 $cm^3\,min^{-1}$. Ellipses are fitted to all 27 sufficiently visible interference patterns.

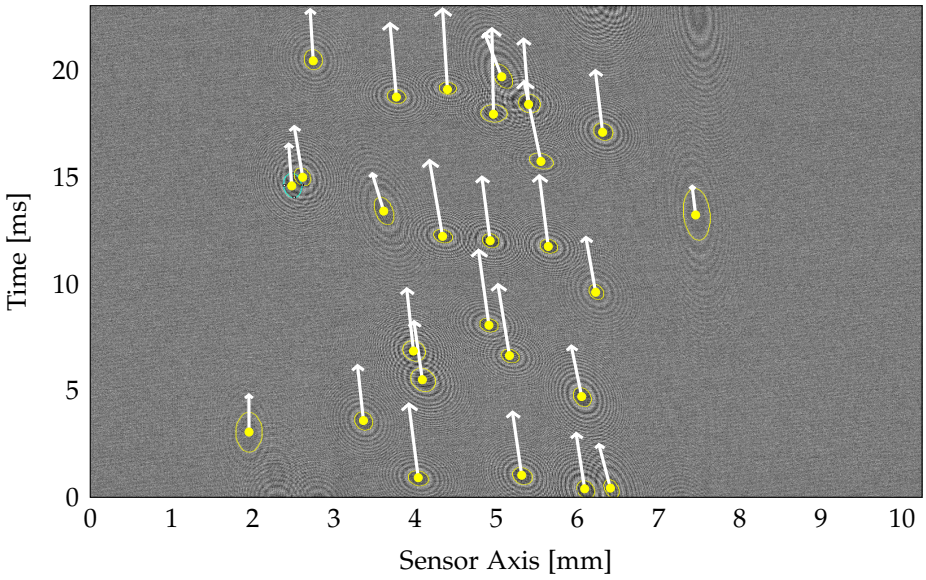

Figure 3.13.: Overlay of the velocity vectors of the particles. The length of the vectors is in arbitrary units but their relative sizes are correct. For the ordinate one unit length of the vector is 1 mm, while the same unit length is 5 ms for the abscissa.

Table 3.1.: Recorded and calculated data for the particle velocity determination.
a, b... Main axes of fitted ellipses
φ... Tilting angle of fitted ellipse
h, w... Apparent height and width of ellipses
d... Apparent diameter of ellipses
v_x, v_y... Velocity in x- and y-Axis
v... Mean velocity

No.	a	b	φ [°]	h	w	d	v_x [m s^{-1}]	v_y [m s^{-1}]	v [m s^{-1}]
1	31.6	24.1	18.8	30.9	−4.2	24.6	0.06	0.35	0.35
2	35.5	23.5	13.4	35.0	−4.6	23.8	0.06	0.30	0.30
3	36.2	21.1	10.6	35.8	−4.3	21.4	0.05	0.26	0.26
4	39.8	21.0	11.7	39.2	−5.8	21.4	0.06	0.24	0.25
5	30.5	17.5	11.9	30.1	−4.2	17.8	0.06	0.26	0.26
6	28.8	21.2	16.2	28.3	−3.6	21.6	0.06	0.33	0.34
7	29.4	19.7	12.2	29.0	−3.4	19.9	0.05	0.30	0.30
8	35.9	23.5	10.3	35.6	−3.7	23.7	0.04	0.29	0.29
9	36.7	19.7	9.6	36.3	−4.3	19.9	0.05	0.24	0.24
10	29.3	22.8	13.4	29.0	−2.6	23.0	0.04	0.35	0.35
11	28.8	21.6	25.7	27.6	−5.1	22.6	0.08	0.36	0.36
12	24.6	20.9	14.8	24.3	−1.7	21.1	0.03	0.38	0.38
13	40.9	22.5	3.6	40.9	−1.8	22.6	0.02	0.24	0.24
14	57.0	22.3	11.0	56.1	−9.2	22.6	0.07	0.18	0.19
15	28.7	22.0	21.3	27.9	−4.1	22.6	0.06	0.35	0.36
16	50.9	21.8	16.6	49.2	−11.8	22.5	0.10	0.20	0.22
17	28.9	20.9	20.1	28.0	−4.6	21.5	0.07	0.33	0.34
18	37.6	22.0	7.3	37.4	−3.1	22.1	0.04	0.26	0.26
19	80.4	32.1	0.1	80.4	−0.2	32.1	0.00	0.17	0.17
20	48.2	29.5	10.9	47.6	−5.7	29.9	0.05	0.27	0.28
21	41.7	27.5	9.7	41.3	−3.9	27.8	0.04	0.29	0.29
22	105.2	32.5	3.1	105.0	−5.1	32.5	0.02	0.13	0.14
23	35.3	26.2	33.6	32.8	−7.8	28.2	0.10	0.37	0.39
24	38.2	26.6	8.2	38.0	−2.8	26.8	0.03	0.31	0.31
25	35.4	32.5	8.4	35.3	−0.8	32.6	0.01	0.40	0.40
26	37.9	17.2	11.7	37.3	−6.1	17.5	0.07	0.20	0.22
27	49.2	22.1	3.1	49.1	−2.1	22.1	0.02	0.20	0.20

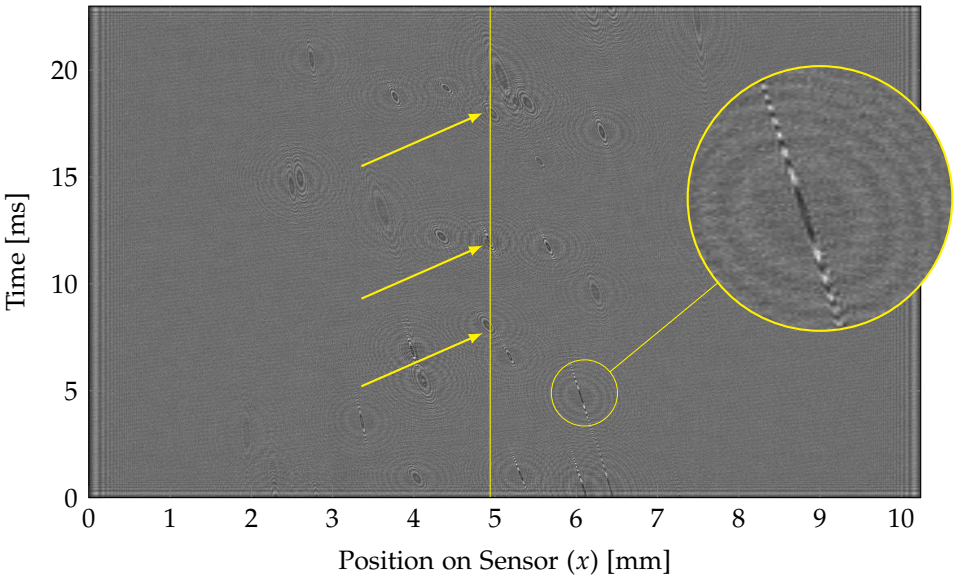

Figure 3.14.: Reconstruction 20.1 mm before the sensor plane. The yellow line shows the position of the cross-section, 5 mm in the sensor plane, displayed in figure 3.15.

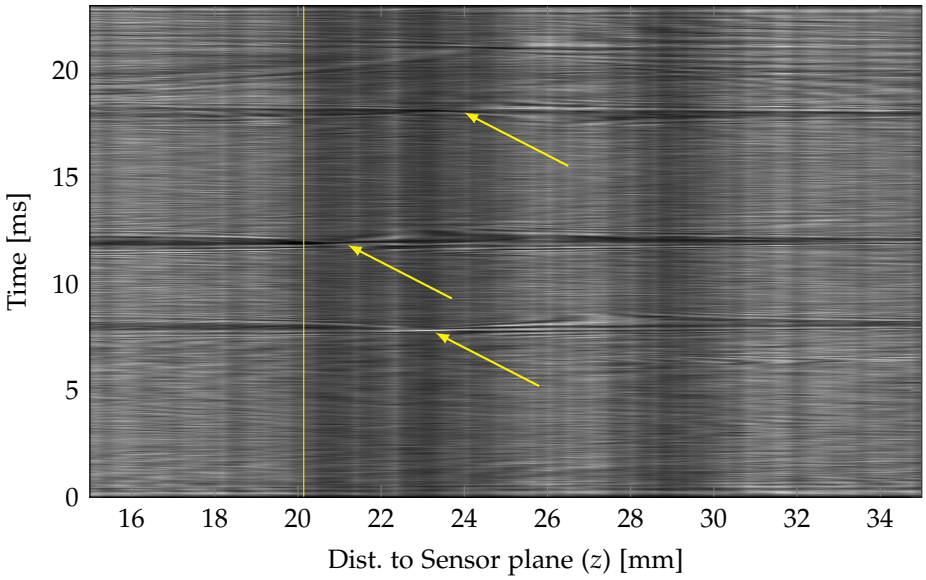

Figure 3.15.: Orthogonal view, 5 mm in the sensor plane. The yellow line shows the position of the cross-section, 20.1 mm before the sensor plane, displayed in figure 3.14.

observed in section 3.4. Nevertheless, the reconstructed interference rings reach a minimum in one dimension at the position of the particle in the reconstruction axis (z-axis), this is shown for one particle in the magnified area of figure 3.14.

The position of the particles in the reconstruction axis can now be obtained by finding the size minimum in one dimension for each particle. This was done manually by creating an easily browseable image stack with the 1000 reconstructed images in *ImageJ*, which was then searched for the minimum of each particle. The process of finding the minima is illustrated by figure 3.14 and figure 3.15, the first picture shows a line which intersects three interference fringes nearly at their center (marked by arrows). The second picture shows the orthogonal cross-section at this line (z-t plane), marking the positions of these three particles in the reconstruction axis with arrows.

The found positions in the z-axis are listed in table 3.2. Additionally, also the positions of the particles in the sensor axis and the relative acquisition time are listed. There is also a column "r" which lists the distance of the particles from the center of the outlet pipe in the x-z plane. The position of this center was determined to be at 4.7 mm in the sensor axis and 22.5 mm in the reconstruction axis (The determination of this center will be explained in section 3.6.4).

3.6.3. Three-dimensional depiction of the particle positions within the pipe

The position and velocity information obtained in section 3.6.1 and section 3.6.2 can be used to show the particle positions in the pipe as they most likely had been before their passing through the detection plane (figure 3.16). In the y-axis this was done by multiplying the particle recording time with the velocity in y-direction, the positions in the x-axis were corrected with the velocity in x multiplied with the recording time. This calculation assumes that the particles velocity vectors did not change between the start of the image acquisition to the detection of the particle.

Figure 3.16 also reveals that the particles closer to the center tend to have higher velocities than those further outside, this suggests that the particles are traveling in an air flow with a laminar flow profile.

Table 3.2.: Data of particle position determination.
x... Particle center position in x and t-axis of image
t... Time of particle acquisition
z... Particle position in z-axis (hologram reconstruction)
r... Distance of particle from the center of the outlet pipe

No.	x [mm]	t [ms]	z [mm]	r [mm]
1	4.1	0.9	23.6	1.3
2	5.4	1.0	20.5	2.1
3	6.2	0.4	20.5	2.4
4	6.2	4.7	20.5	2.4
5	6.4	9.6	24.0	2.1
6	5.8	11.7	21.3	1.5
7	5.0	12.0	21.1	1.4
8	6.5	17.1	22.0	1.7
9	2.7	15.0	22.9	2.1
10	3.9	18.7	21.7	1.2
11	4.4	12.2	23.2	0.8
12	4.5	19.1	21.8	0.8
13	2.8	20.4	21.8	2.1
14	3.7	13.4	25.6	3.3
15	5.0	8.0	23.5	1.0
16	5.2	19.7	24.9	2.4
17	5.3	6.6	20.9	1.7
18	3.4	3.6	21.0	2.0
19	2.0	3.0	24.1	3.2
20	4.2	5.5	24.5	2.1
21	4.1	6.8	20.9	1.8
22	7.6	13.2	23.1	2.8
23	5.7	15.7	21.7	1.2
24	5.5	18.4	23.6	1.3
25	5.1	17.9	23.5	1.0
26	6.6	0.4	20.3	2.8
27	2.5	14.6	22.2	2.2

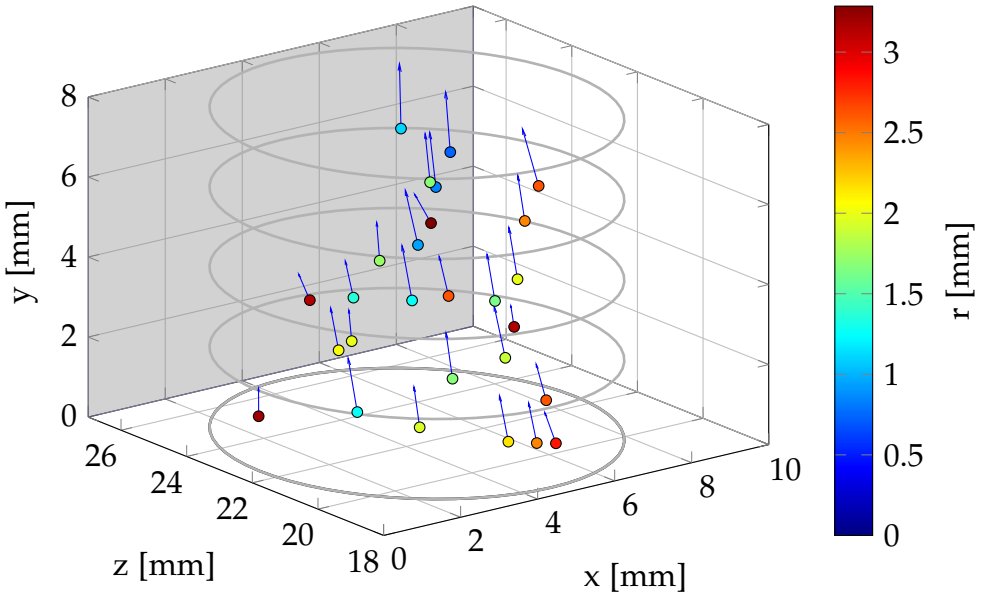

Figure 3.16.: Probable positions of the particles inside the pipe right before passing through the detection plane. The vectors show the velocities in the x-y-pane. The colours of the particles indicate the distance r from the centre of the pipe.

3.6.4. Flow rate determination

In section 2.2.1 it has already been determined that the flow profile of the aerosol that exits the pipe, has to be laminar because of the low Reynolds number. The following equation determines the velocity profile $v(r)$ of a laminar flow inside of a round pipe (chapter 4 of [36]):

$$v(r) = \frac{2 \cdot q_V}{\pi \cdot R^4} \cdot (R^2 - r^2) \tag{3.16}$$

r...Radius [m]
R...Radius of pipe [m]
q_V...Volumetric flow [$m^3\,s^{-1}$]

This polynomial equation was fitted with a least-square algorithm to the known velocities v_y in y-direction: First the distance r of each particle to the center in the detection (x-z) plane was determined (already displayed in table 3.2), then (3.16) was fitted to the measured velocities $v(r)$ with an *Octave*-Script called *mmpolyfit* [19]. This script allows for polynomial fitting with additional

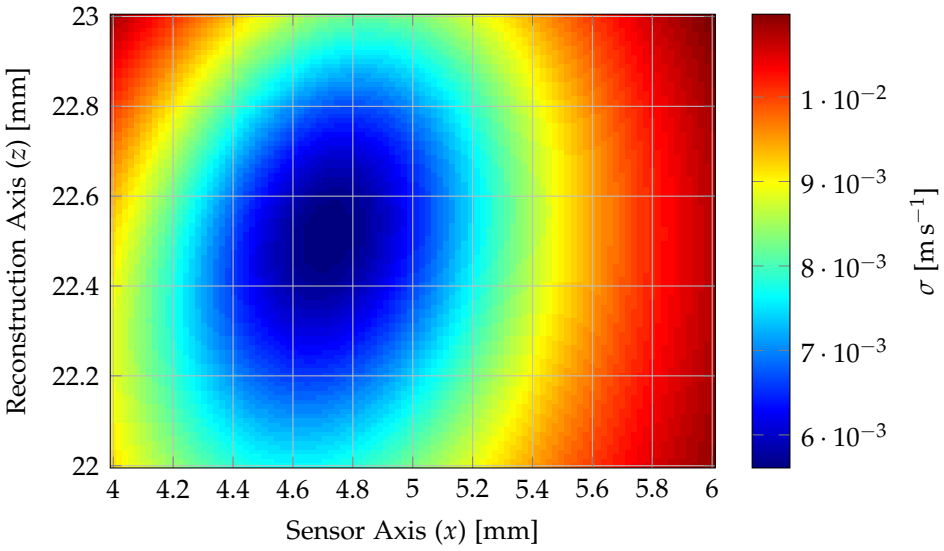

Figure 3.17.: Standard deviation σ of fitted laminar flow depending on the chosen center coordinates. 4.7 mm in the sensor axis and 22.5 mm in the reconstruction axis is the optimal center position.

constraints, the additional constraint in this case being a derivative of zero at the center of the pipe. This is necessary because otherwise there would always be a kink in the center of the flow profile.

Center determination

Since the outlet pipe was flexible and not tightly fixed, it could occur that the position of the center varied slightly between the recorded holograms. To get a reliable measurement for the center position without measuring the geometry with a caliper after each hologram acquisition, the center coordinates have been determined by calculating the least square fits of (3.16) as described before for a matrix of 100×100 center coordinates, ranging from 4 mm to 6 mm on the sensor axis and from 22 mm to 23 mm on the reconstruction axis.

The standard deviation σ of the measured values to the fitted ones was then plotted as is shown in figure 3.17. The position of the minimum standard deviation was determined as the center of the blue area. It was found to be at 4.7 mm in the sensor axis and 22.5 mm in the reconstruction axis. It can be assumed that this also is the center of the outlet pipe.

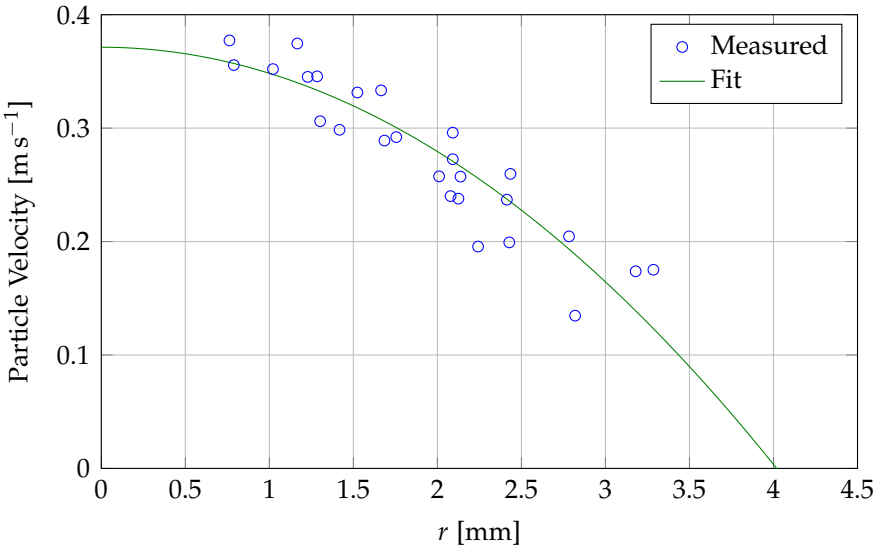

Figure 3.18.: Measured absolute particle velocities and fitted laminar flow profile as a function of the distance from the centre of the pipe r.

Flow rate determination

Figure 3.18 shows the flow profile fitted with the optimal center coordinates. The volumetric flow rate for this profile is $q_{fit} = 565\,\mathrm{cm}^3\,\mathrm{min}^{-1}$. The flow rate measured with the MFM (in section 3.6.1) was $q_{MFM} = 595\,\mathrm{cm}^3\,\mathrm{min}^{-1}$, however in this case the flow rate should be normalized to the correct temperature and pressure with (2.2) for better comparability. The temperature of the aerosol at the detection plane was estimated to be at approximately $T = 25\,^{\circ}\mathrm{C}$, the ambient pressure was $p_{amb} = 980\,\mathrm{mbar}$. This gives a correction factor of 1.048, the flow rate corrected with this factor is $q_{MFMcor} = 624\,\mathrm{cm}^3\,\mathrm{min}^{-1}$.

The flow rate measured with the MFM and the flow rate determined by the velocities of the 27 particles are thus within 10 %, which is a very satisfying result considering the complexity of the later method.

The second result that can be obtained out of the fit of (3.16) is the approximate diameter of the pipe, it has to be the first root of the polynomial. In figure 3.11 it is visible that this root is at $r = 4\,\mathrm{mm}$, thus the diameter is $d = 8\,\mathrm{mm}$. This corresponds to the inner diameter of the outlet tube of 7.8 mm and is thus a further evidence that the assumption of fitting the flow profile as explained is feasible.

Finally, figure 3.18 shows, that only very few particles are visible from radius 3 mm to 4 mm. The reason for this can partly be found in the low velocities at the edge of the flow profile, which lead to fewer recorded particles in the same time during the hologram recording. However, it can be assumed that the low number of particles in this area is also partly due to the fact that the diameter of the condenser outlet pipe is extended from 5 mm to 7.8 mm as explained in section 2.1.1. The gas flow adapts to the larger diameter nearly immediately, but the particles cannot follow as fast.

4. Particle diameter determination with Static Light Scattering

The diameter of the particles that exit the CNM was determined to be in the range of 10 µm in section 3.4.1. A more precise size determination was not possible with the current holography setup, thus it was decided to use Static Light Scattering (SLS), a standard method for the characterization of small particles, to measure the particle diameters.

The diameter of the condensed droplets was not only of interest to confirm the size results obtained with hologram reconstruction, but also to gain a deeper understanding of the operating properties of the CNM. Additionally, it was also of interest to confirm the particle size that was estimated with a computer simulation as mentioned in section 2.1.1.

4.1. Principle of Static Light Scattering

The basic principle of SLS is to illuminate a sample (particles) with a monochromatic light source of a certain wavelength λ and then measure the intensity $I(\Theta)$ of the scattered light dependent on the scattering angle Θ (i.e. the angle between incident and scattered light, see figure 4.2) [32].

Much information can be obtained out of this scattering curve, e.g. the molecular weight, shape, and size of the sample. The main interest of this work was the determination of the particle size.

It can be extracted out of the slope of a *Guinier Plot* as well as from the minima of the Intensity curve, this will be explained in the following sections.

4.1.1. Guinier Plot

The Guinier plot shows the logarithmized intensity $\ln(I(\Theta))$ as a function of the squared scattering vector q^2. The scattering vector is defined as follows [32]:

$$q = \frac{4\pi n_0}{\lambda} \cdot \sin\left(\frac{\Theta}{2}\right) \tag{4.1}$$

n_0...Refractive index of the solvent
λ...Wavelength of the incident light
Θ...Scattering Angle

The slope of the first intensity decrease ($\Delta \ln(I)/\Delta q^2$) of the scattering curve gives a very good estimation for the *Radius of Gyration*, R_g:

$$R_g = \sqrt{-3 \cdot \frac{\Delta \ln(I)}{\Delta q^2}} \tag{4.2}$$

Since the particles are "massive" spheres due to the fact that they are fluid droplets at a low flow speed, the following equation can be used to calculate the physical radius R of the particles out of the radius of gyration:

$$R = \sqrt{\frac{5}{3}} \cdot R_g \tag{4.3}$$

4.1.2. Scattering curve of a sphere

The scattering curve $I(q, R)$ of a single sphere with radius R can be expressed with [3]:

$$I(q, R) = \left(3 \cdot \frac{\sin(qR) - qR\cos(qR)}{(qR)^3}\right)^2 \tag{4.4}$$

Figure 4.1 shows a scattering curve calculated with (4.4) for a sphere with a radius of 3.5 µm, this radius has been chosen because it corresponds to the diameter expected by the computer simulations (section 2.1.1) of 7 µm.

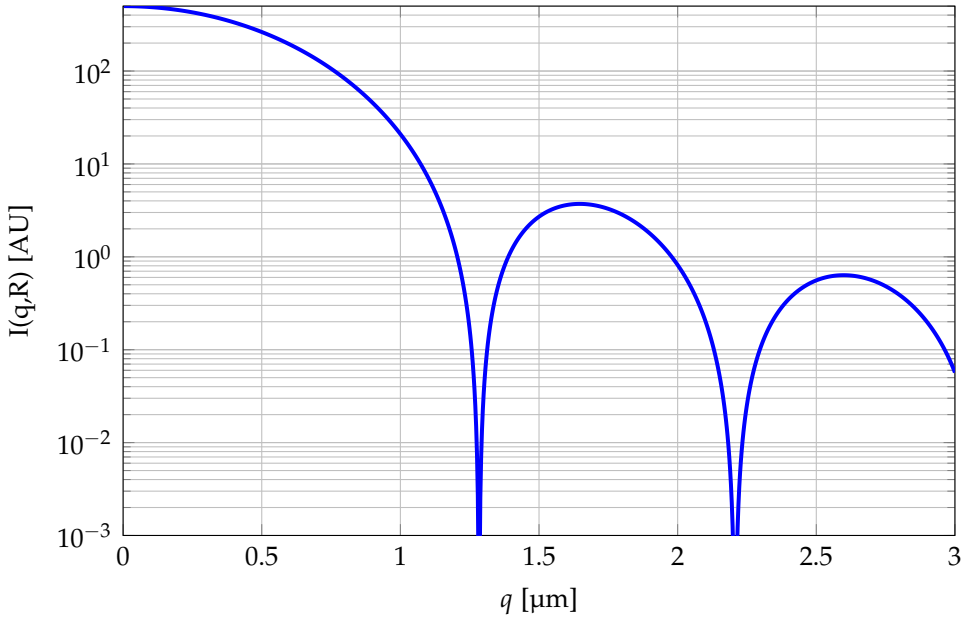

Figure 4.1.: Calculated scattering curve of a single sphere with a radius of 3.5 µm.

The positions of the minima of the scattering curve q_{zi} can now be used to determine the radius R of the sphere. The following equation shows the numerical solution for the first two minima:

$$R \approx \frac{4.493}{q_{z1}}, \quad R \approx \frac{7.725}{q_{z2}} \tag{4.5}$$

This estimation is only valid if the scatterers are spheres of a monodisperse size distribution, otherwise the minima will not be very distinctly.

4.2. Experimental Setup

The SLS apparatus was custom built, mainly with components from *Thorlabs Inc.*. Some adapters had to be constructed and milled. This SLS apparatus was then installed on top of the CNM.

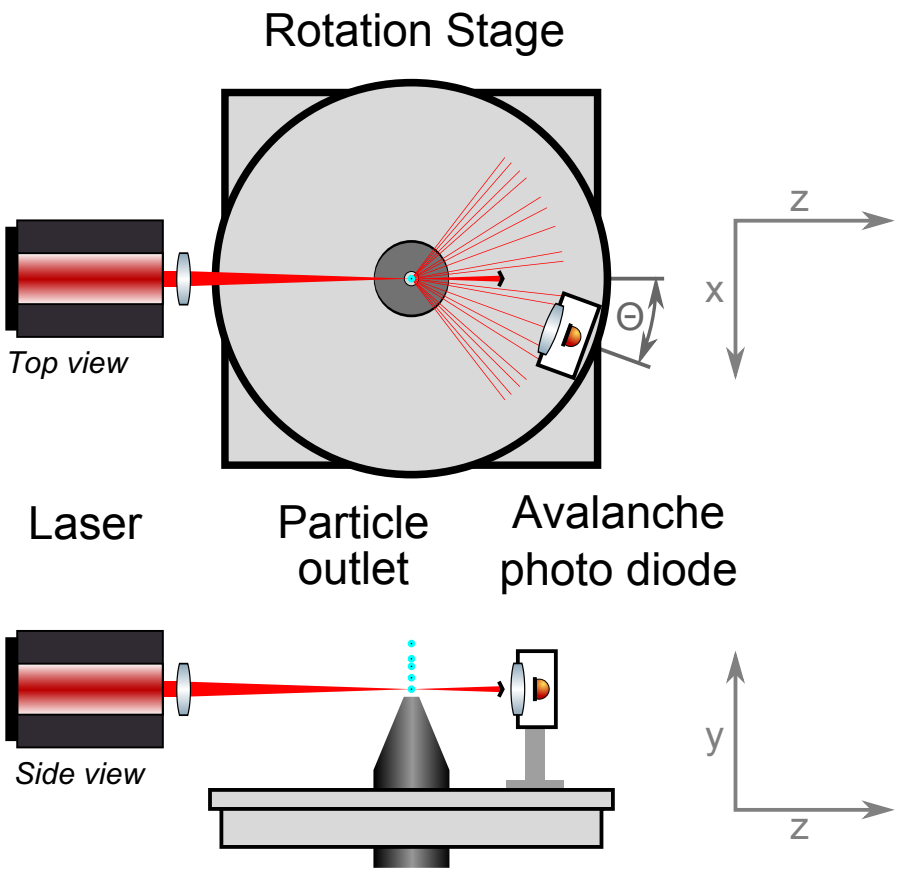

Figure 4.2.: Schematic of the Static Light Scattering - setup.

4.2.1. Components of the Static Light Scattering apparatus

Figure 4.2 shows the schematic, figure 4.3 an image of the SLS setup: It consists of a Laser, a Rotation Stage with the Particle outlet in the center and detector optics, namely a convex lens, an aperture and the photodetector, an Avalanche Photo Diode (APD).

The following components were used:

Laser: Adjustable focus laser diode by *Thorlabs Inc.* [22]:

Identifier: CPS196
Wavelength: $\lambda = 635\,\text{nm}$
Power: 4.5 mW
Laser Class: 3R
Focus: Adjustable, 50 mm to infinity
Beam diameter when collimated: $\perp$ 2.45$\times$ $\parallel$ 0.54 mm
Beam divergence when collimated: $\perp$ 0.6 mrad, $\parallel$ 1.8 mrad

APD: Avalanche Photo Diode by *Thorlabs Inc.* [21]:

Identifier: APD120A2/M
Wavelength Range: $400 - 1000\,\text{nm}$
Detector active area diameter: 1 mm
Output Bandwidth: $0 - 50\,\text{MHz}$

Lens: Plan-convex lens by *Qioptiq*:

Identifier: G063103322
Focal length: 80 mm
Diameter: 31.5 mm

Aperture: Zero Aperture Iris by *Thorlabs Inc.*:

Identifier: SM1D12SZ
Aperture diameter: adjustable, 0 – 12 mm

Rotation Stage: XY Translation Stage with Rotating Platform by *Thorlabs Inc.*:

Identifier: XYR1/M
Rotation: 360° continuous rotation, 1° markings, fixable.
Translation: Micrometers for X and Y, 10 µm graduations.

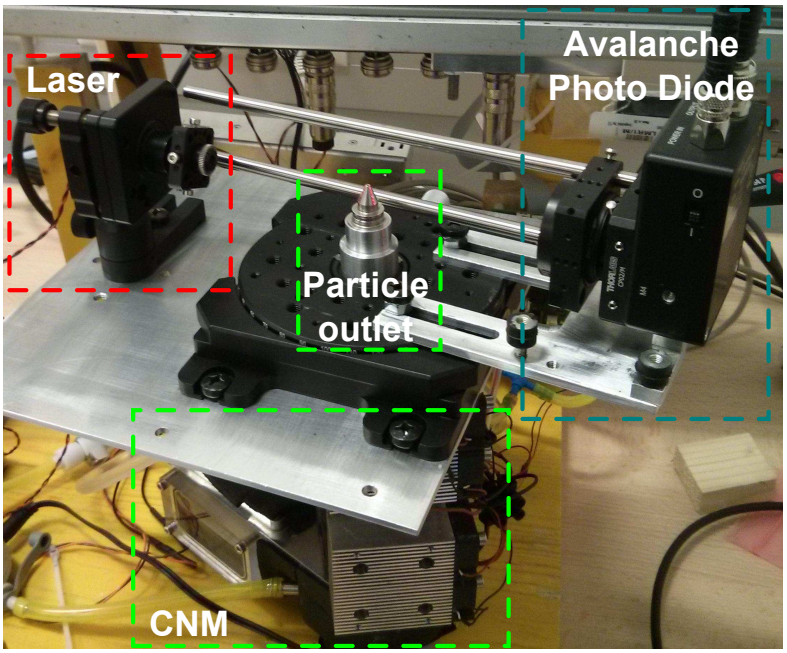

Figure 4.3.: Image of the Static Light Scattering - setup.

4.2.2. Description of the Static Light Scattering apparatus

As shown in figure 4.2 and 4.3, the laser was mounted outside the rotation stage. The focus was set to 85 mm, the center position of the rotation stage. In this center the particle outlet, being a nozzle with an inner diameter of 0.5 mm, was placed. The particle outlet was connected to the transfer tube of the CNM (section 2.1.1). On the rotating platform an adapter was placed to hold the APD housing. In front of the APD the iris aperture was mounted, followed by the planoconvex lens. The distance between particle outlet and the center of the lens was set to $f = 80\,\text{mm}$, the focal length of the lens. Since the APD had an active area diameter of $d = 1\,\text{mm}$ and the incident light from the scattering center above the nozzle was collimated by the planoconvex lens, the collection angle of the apparatus was:

$$\phi = 2 \cdot \arctan\left(\frac{d/2}{f}\right) = 0.72^\circ \tag{4.6}$$

The beam stop shown in figure 4.2 was not realized as depicted; instead the iris aperture was used to protect the APD of any stray light. The minimum

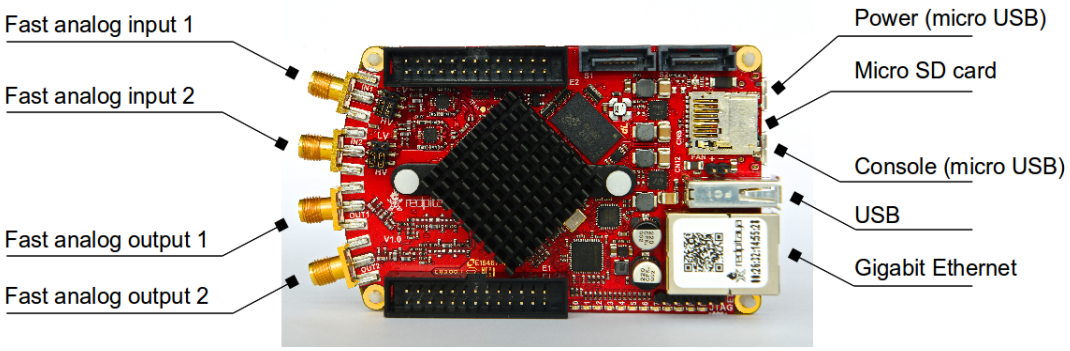

Figure 4.4.: Red Pitaya - an open source measurement and control tool [6].

scattering angle that could be measured with this setup without damaging the APD was $\Theta_{min} = 1.5°$.

The precise position adjustment of the particle outlet relative to the laser beam was performed with the micrometers of the translation stage.

4.2.3. Data acquisition

The APD provides a voltage signal with a maximum frequency of 50 MHz as an output. For the measurement of this signal a *Red Pitaya* [6] was available. This is an open-source measurement and control tool. Basically, it is a circuit board (figure 4.4) that contains two 50 MHz (=125 MSps) inputs and two 50 MHz outputs, as well as a Field Programmable Gate Array (FPGA) and a dual-core ARM CPU, which is used to run a *Linux* operating system.

The great advantage of this system is the flexibility of having a simply programmable high-frequency data acquisition device which can easily be connected to a computer but can also be used standalone. For the SLS setup it was used as a signal integrator.

An exemplary C-program for direct signal acquisition was modified to add the functionality of an integrator. This program reads the contents of a 16 kB circular sample buffer which is updated by the Analog Digital Converter (ADC) with the current sampling frequency and calculates a sum over the samples. The best way of implementing such an integrator would have been to program the FPGA to make this calculation, because FPGAs are built for high-speed low level calculations. However, since the know-how for FPGA programming had

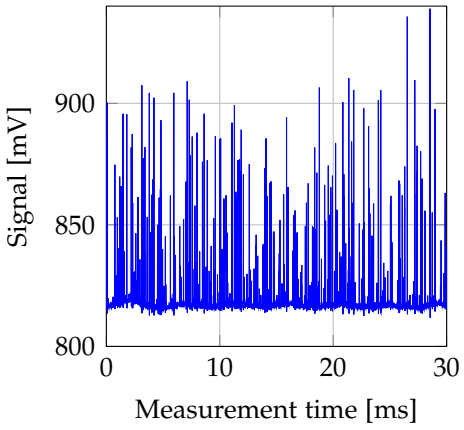

Figure 4.5.: Intensity signal at a scattering angle of 1.5°. All visible peaks are particles.

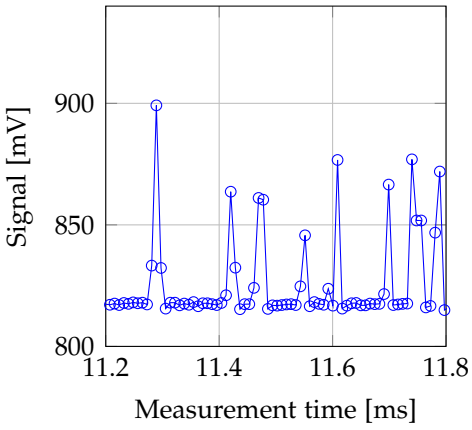

Figure 4.6.: Detail of the raw signal. The circles show the position of the recorded data points.

not been available at this time, it was decided to modify the aforementioned program which now runs on the ARM CPU.

The main disadvantage of this approach was the following: At high sample rates the CPU was not fast enough to integrate over all samples continuously. A sample rate of 122 kSps was found to be the optimal compromise between speed and efficiency, as it was still sufficiently fast but also allowed for integration at 85 % of the runtime.

Data evaluation was done in *GNU Octave*, the interface to the Red Pitaya was realized via Secure Shell (SSH) over Ethernet. This means that it was possible to execute command line programs on the Red Pitaya from the Octave scripts running on the control computer.

4.3. Experiments

4.3.1. Approach

The flow rate through the system was set to 500 $\mathrm{cm}^3\,\mathrm{min}^{-1}$ in order to create similar experimental conditions as in section 3.4, where the particle size was estimated with holography.

The aerosol source was again ambient air as described in section 2.1.2. Figures 4.5 and 4.6 show the signal of the APD for a measurement at a scattering angle of 1.5°, and at the sample rate of 122 kSps. It shows clearly that this rate is still sufficient to see the peaks of the single particles.

The signal as seen in figure 4.5 was now integrated over an integration time of 54 s, with the efficiency of 85 % stated in section 4.2.3. This means that the effective measurement time was 63 s. Each intensity measurement at a scattering angle Θ now consisted of such an integral $I_p(\Theta)$ with particles flowing through the nozzle and one without particle flow, measuring the background light intensity $I_b(\Theta)$.

The relative intensity $I_R(\Theta)$ was then calculated by subtracting the background from the particle signal:

$$I_R(\Theta) = I_p(\Theta) - I_b(\Theta) \tag{4.7}$$

Since the resolution of the angle markings on the rotation stage was 1°, it was decided that the highest approximately adjustable angle resolution is $1/3°$. Of course, this already has an error of at least $\pm 0.1°$.

Measurements at a certain angle were always repeated at least four times, the angle setting of the rotation stage had always been re-set beforehand to get a better estimation of the measurement error. The relative intensity values were averaged for each angle, the error was calculated as two times the standard deviation σ of this average (=95 % within confidence interval).

4.3.2. Results

Table 4.1, figure 4.7 and figure 4.8 show the results of the light scattering experiment. The scattering vector in figure 4.8 was calculated with (4.1), the wavelength was $\lambda = 635\,\text{nm}$, the refractive index of the solvent (=Air) $n_0 = 1$. The error bars show the aforementioned confidence interval of 95 %.

4.3.3. Problems with the setup

The error bars in figure 4.8 are relatively large, this is due to the following problems with the setup:

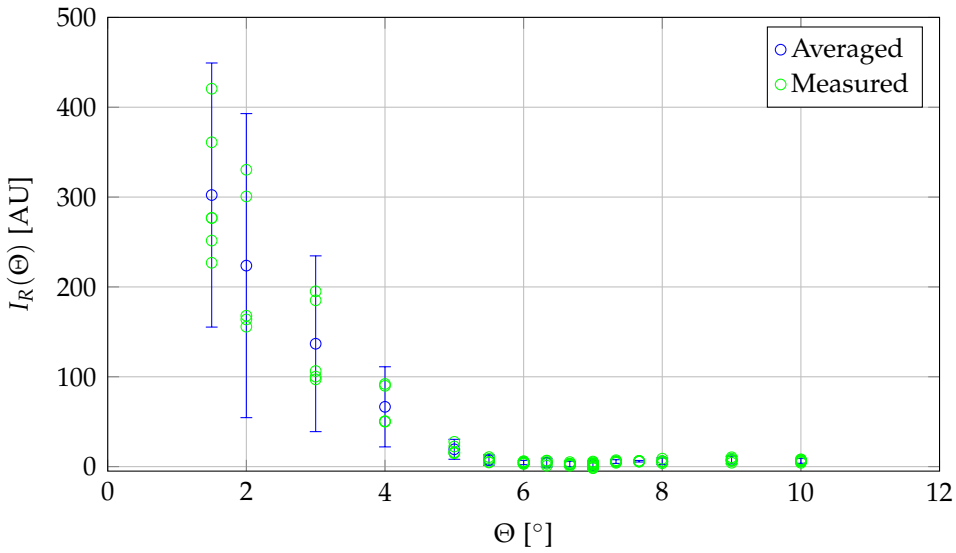

Figure 4.7.: Measured relative intensities as a function of the scattering angle.

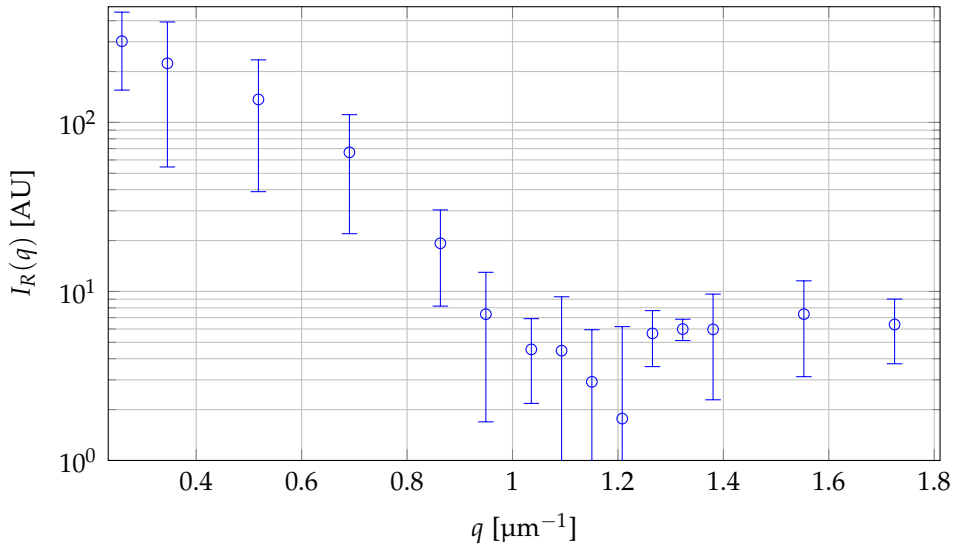

Figure 4.8.: Measured averaged relative intensities as a function of the scattering vector on a semilogarithmic plot.

Table 4.1.: Measurement results of the Static Light Scattering-experiment.
Θ... Scattering angle
q... Scattering vector (4.1)
I_R... Relative intensity
2σ... Double standard deviation
n_m... Number of measurement repetitions

Θ [°]	q [µm^{-1}]	I_R	2σ	n_m
1.5	0.259	302.3	147.0	6
2.0	0.345	223.7	169.2	5
3.0	0.518	136.8	97.8	5
4.0	0.691	66.6	44.6	5
5.0	0.863	19.3	11.1	5
5.5	0.949	7.3	5.6	4
6.0	1.036	4.5	2.4	6
6.3	1.093	4.5	4.8	5
6.7	1.151	2.9	3.0	5
7.0	1.208	1.8	4.4	14
7.3	1.266	5.6	2.1	5
7.7	1.323	6.0	0.9	4
8.0	1.380	6.0	3.7	5
9.0	1.553	7.3	4.2	6
10.0	1.725	6.4	2.6	7

1. The particle number concentration in the laboratory was not always constant. For a more precise measurement it would have been necessary to measure the concentration continuously with a CPC in parallel and then correct all intensity integrals with the measured concentrations.
2. It was not possible to darken the laboratory completely, thus the ambient light intensity was not constant at all times. It would have been better to build an enclosure for the whole optics setup.
3. The nozzle was not perfectly centered relative to the pivot of the rotation stage due to mechanical issues. A better nozzle holder would have been preferable.
4. No reference detector was used to monitor the output intensity of the laser, thus it had to be assumed that the intensity was constant over the measurement time.

Despite these problems the results of the measurements were still of sufficient precision to determine the particle diameter.

4.3.4. Diameter estimation with Guinier plot

Figure 4.9 shows the Guinier plot (as described in section 4.1.1) of the measured data. A linear fit through the first nine acquired scattering angles was calculated; the slope was then used to calculate the radius of gyration with (4.2) to $R_g = 3.4\,\mu m$. The error was estimated to $\Delta R_g = 0.3\,\mu m$ by calculation of two worst case slopes that are still within the 95 % prediction interval. The physical radius obtained with (4.3) is then $R = (4.4 \pm 0.4)\mu m$.

The diameter of the particles determined with the Guinier plot is thus:

$$D_{GU} = (8.8 \pm 0.8)\mu m$$

This matches the estimated size of $< 10\,\mu m$ in section 3.4.1 as well as the size of $(7 \pm 2)\,\mu m$ determined by computer simulation in section 2.1.1 nicely.

4.3.5. Diameter estimation with the first minimum of the scattering curve

Equation (4.5) was used to calculate the radius out of the first minimum of the scattering curve (figure 4.8, table 4.1). Since three measured values were within

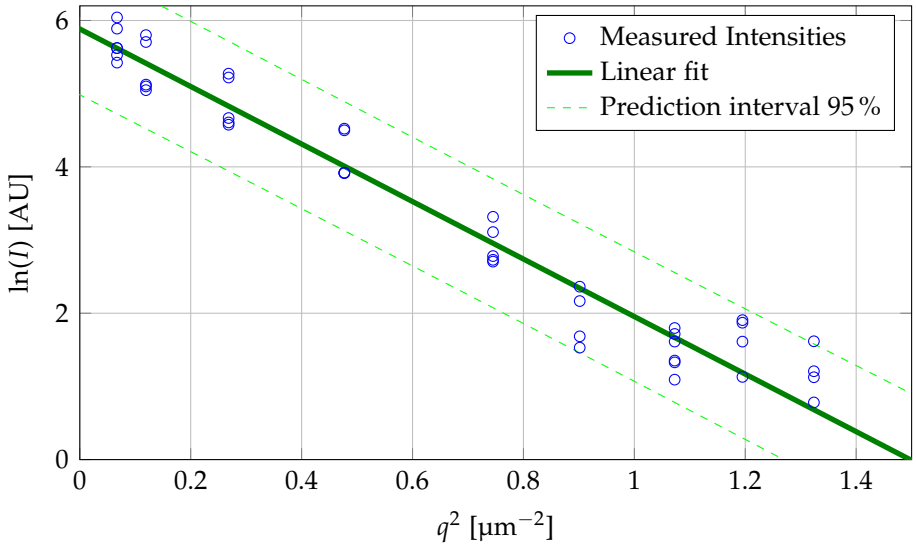

Figure 4.9.: Guinier plot with linear fit of the measured data.

the possible range of being the minimum (in the 95 % confidence interval), the radius was estimated to be within the range of the results obtained out of these very minima. Table 4.2 shows the calculated radii.

Table 4.2.: Radii obtained from first minimum of scattering curve.
q...Scattering vector
R...Obtained radius

q [µm^{-1}]	R [µm]
1.093	4.1
1.151	3.9
1.208	3.7

The diameter of the particles obtained with the "Minimum Method" is thus:

$$D_{MM} = (7.8 \pm 0.4)\text{µm}$$

This matches the results of section 4.3.4 as well as the simulation results (section 2.1.1).

In figure 4.10 possible scattering curves were fitted to the measured data. The intensities were calculated with (4.4), as radii the results from table 4.2 were

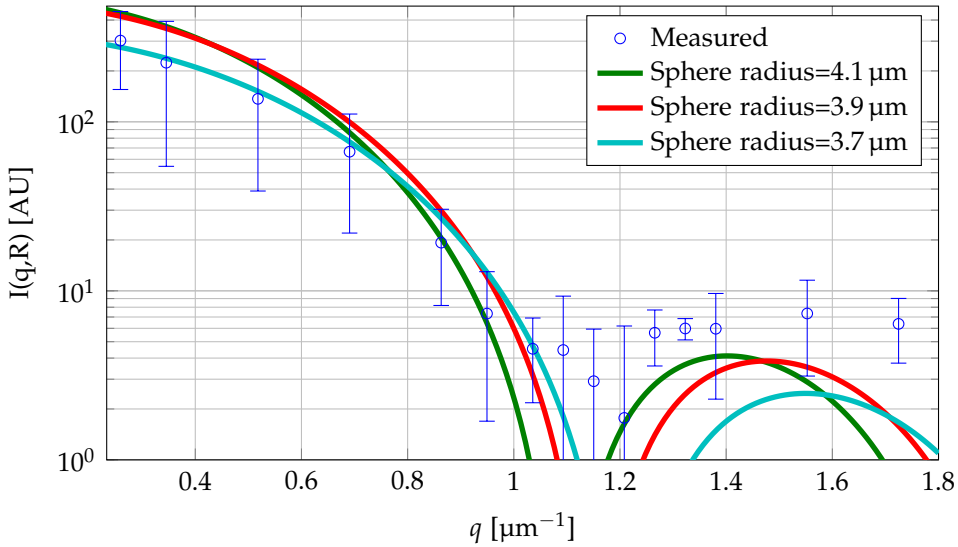

Figure 4.10.: Measured data and calculated scattering curves for the radii obtained from the three possible minima.

used. The scattering curves were scaled to different maximum intensities with the aim of fitting the curves into the highest number of data points.

All curves fit the first decent until $q \approx 1\,\mu m^{-1}$ sufficiently, subsequently the fit for $R = 3.9\,\mu m$ shows the best match, which is however not as well as for the first decent. The fact that a minimum is visible in the measured data at all implicates that the size distribution of the particles is indeed very narrow. However, since the measured data was desmeared neither for the collection angle of the apparatus (4.6) nor for the positional variation of the particles in the nozzle flow, a scattering curve perfectly resembling that of a monodisperse spherical scatterer cannot be expected.

5. Conclusion and Outlook

The main objective of this work, namely the determination whether the new bright field detection setup as suggested in [8] can be used for the detection of particles as they are produced in a Condensation Particle Counter (CPC), was completed satisfactory. Particles can indeed be detected, the *number of particles* counted with the new setup matches the number of particles counted with a commercial CPC within the respective error margins ($\pm 10\,\%$).

The particles are not only visible as shades in the sensor plane, as the coherent light of the illuminating laser additionally produces interference patterns. This technique is generally known as Digital In-Line Holography (DIH). The holograms produced with DIH can be used to reconstruct the electromagnetic field of the scattered light within the illuminated volume. This enables the determination of the *sizes* and two-dimensional *positions* of the particles within the detection plane with an one-dimensional line sensor. Additionally, the deformation of the interference patterns in the recorded holograms can be used to estimate the *velocity* of the particles. Knowledge of the positions and the velocities of the particles enables the fitting of flow profiles and the determination of the aerosol *flow rate*.

The particle size of the particles exiting the Condensation Nucleus Magnifier (CNM) was estimated with holography to be in the rage of 10 µm (precision limited because of the sensor pixel size). An alternate method for size determination, Static Light Scattering (SLS) was used to determine the particle diameters to be within 7.4 µm and 9.6 µm. Previous computer simulations also resulted in a diameter in this range, i.e. (7 ± 2) µm.

The new setup has optimization potential, namely:

- Sensor pixel size: For increased resolution the sensor pixel size should be reduced to at least 5 µm or even less. This should enable the measurement of the particle sizes with DIH with a higher precision.

- Outlet of the CNM: The diameter of the condenser outlet of the CNM is currently 5 mm, this size should be increased to match the width of the line sensor. This measure would lower the flow velocities, thus allowing for longer exposure times, and also optimize the usage of the sensor area.
- Optics enclosure: A housing sealed against ambient air would prevent ambient dust particles from entering the beam path and producing "false" particle images.

Summing up, for a future CPC, the new setup would provide the following advantages:

- *Particle Number*: Because of DIH, it should be possible to identify and count a very high number of particles simultaneously in the reconstructed volume without having coincidence events.
- *Particle Size*: The monitoring of the particle size would ensure the sufficient functionality of the CNM stage and enable the detection of drifts over time.
- *Particle Velocities*: Monitoring the particle velocities would ensure that clogging or contamination of the flow path can be detected. Additionally no external flow meter would be necessary for the flow rate determination.

All these points assume that there are automatic algorithms available that retrieve the respective measurement values with a sufficiently high update rate. Further work should focus on the development of real time algorithms to calculate the aforementioned parameters. All measurement values reported in this work have been calculated "manually" from the retrieved images.

Appendix

Appendix A.

List of Acronyms

ADC Analog Digital Converter
APD Avalanche Photo Diode
ASM Angular Spectrum Method
CNM Condensation Nucleus Magnifier
CPC Condensation Particle Counter
CVS Constant Volume Sampler
DIH Digital In-Line Holography
DPF Diesel Particle Filter
FFT Fast Fourier Transformation
FPGA Field Programmable Gate Array
GPU Graphics Processing Unit
HEPA High Efficiency Particulate Air
MFM Mass Flow Meter
PM Particulate Mass
PMP Particle Measurement Programme
PN Particle Number
PNC Particle Number Counter
PSL Polystyrene Latex
R83 Regulation 83
SLS Static Light Scattering
SSH Secure Shell
UNECE United Nations Economic Commission for Europe

Appendix B.

Additional images

B.1. Images recorded with the scatter-abatement optics

All concentrations are calculated with (2.7), all variables are named as described in section 2.2.3. The scatter-abatement optics as described in section 2.1.6 were used.

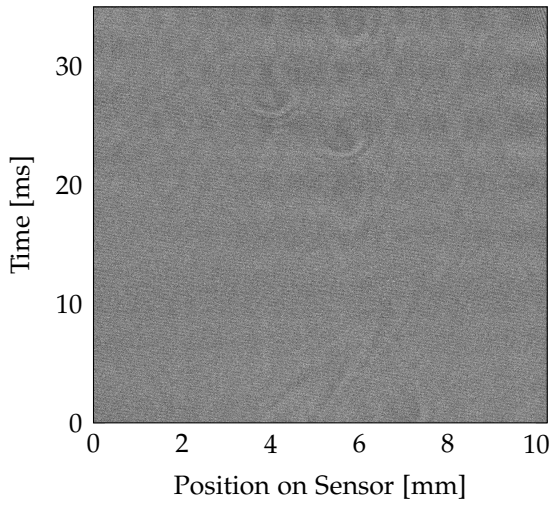

Figure B.1.: q_{MFM}=380 cm^3 min^{-1}, t_s=0.035 ms, n_l=1000, n_P=3. $\Rightarrow$ C_{calc}=14 cm^{-3}; C_{CPC} =(13 $\pm$ 10) cm^{-3}

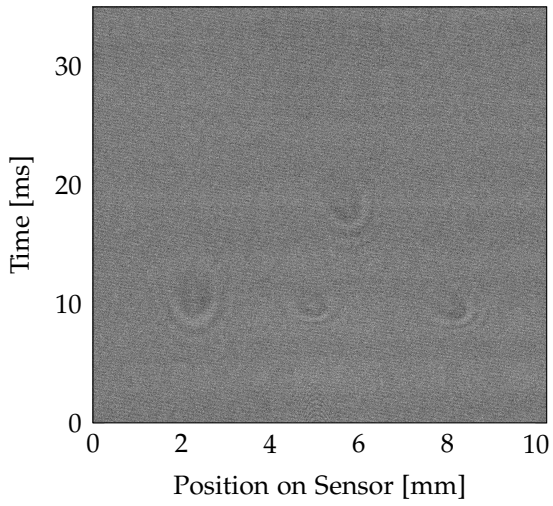

Figure B.2.: q_{MFM}=380 cm^3 min^{-1}, t_s=0.035 ms, n_l=1000, n_P=4. $\Rightarrow$ C_{calc}=18 cm^{-3}; C_{CPC} =(13 $\pm$ 10) cm^{-3}

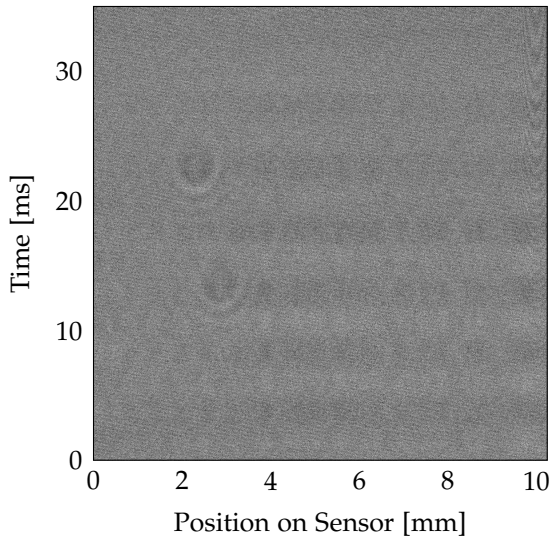

Figure B.3.: q_{MFM}=380 cm^3 min^{-1}, t_s=0.035 ms, n_l=1000, n_P=2. $\Rightarrow$ C_{calc}=9 cm^{-3}; C_{CPC} =(13 $\pm$ 10) cm^{-3}

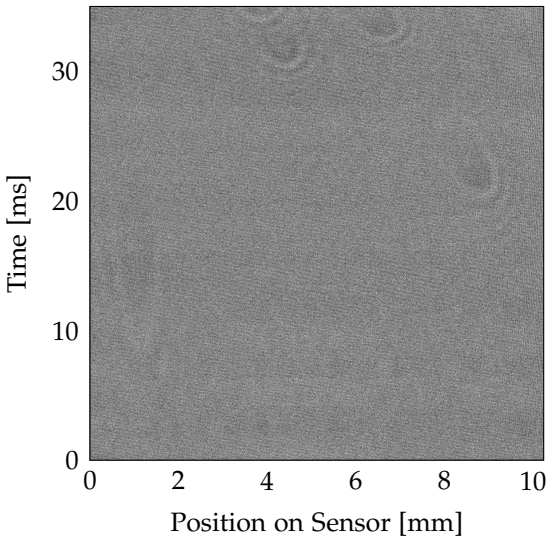

Figure B.4.: q_{MFM}=380 cm^3 min^{-1}, t_s=0.035 ms, n_l=1000, n_P=4. $\Rightarrow$ C_{calc}=18 cm^{-3}; C_{CPC} =(13 $\pm$ 10) cm^{-3}

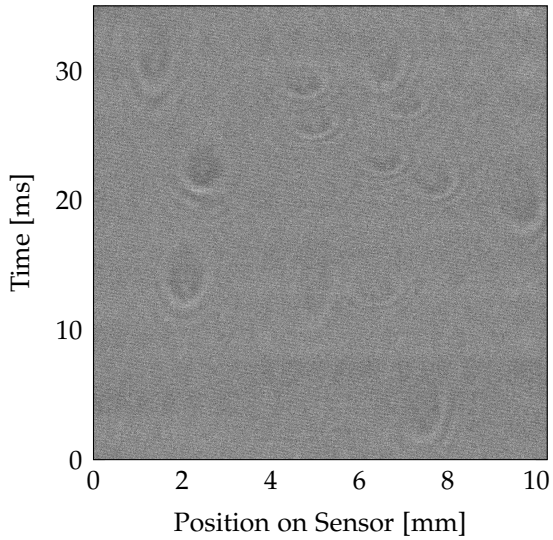

Figure B.5.: q_{MFM}=380 cm^3 min^{-1}, t_s=0.035 ms, n_l=1000, n_P=13. $\Rightarrow$ C_{calc}=59 cm^{-3}; C_{CPC} =(90 $\pm$ 10) cm^{-3}

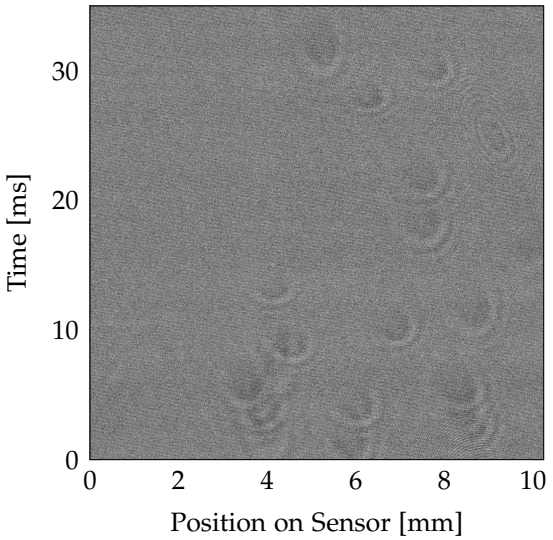

Figure B.6.: q_{MFM}=380 cm^3 min^{-1}, t_s=0.035 ms, n_l=1000, n_P=17. $\Rightarrow$ C_{calc}=77 cm^{-3}; C_{CPC} =(90 $\pm$ 10) cm^{-3}

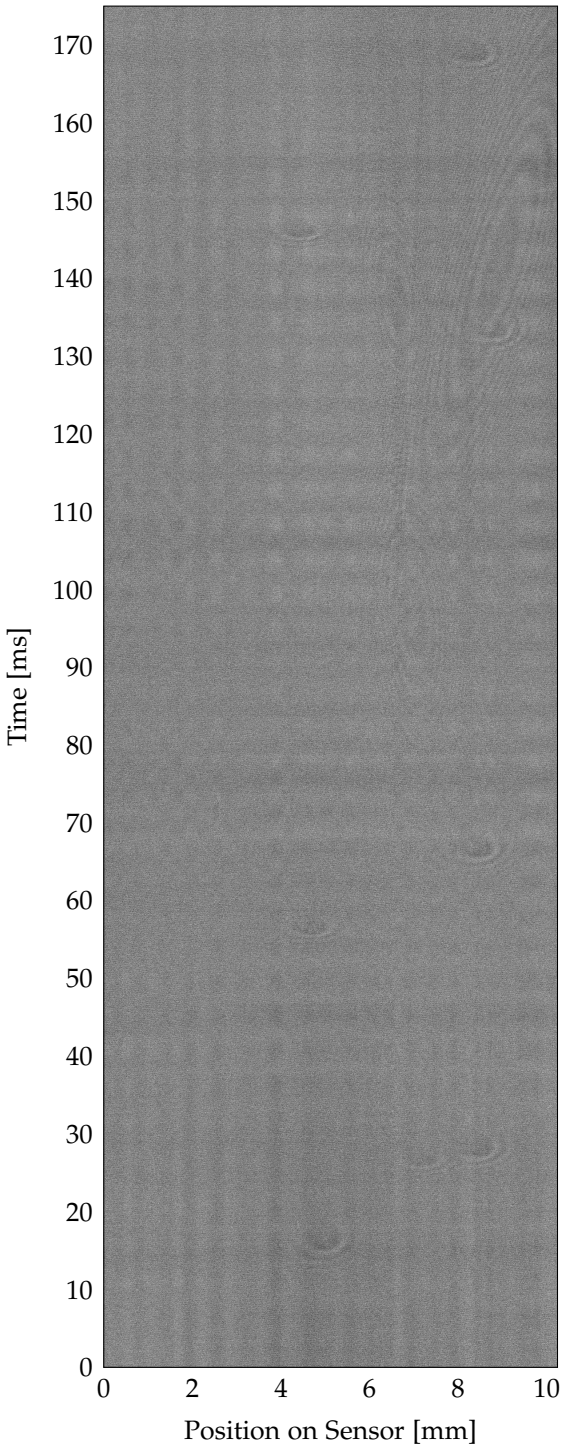

Figure B.7.: q_{MFM}=380 cm^3 min^{-1}, t_s=0.035 ms, n_I=5000, n_P=8. $\Rightarrow$ C_{calc}=7 cm^{-3}; C_{CPC} =(9 $\pm$ 10) cm^{-3}

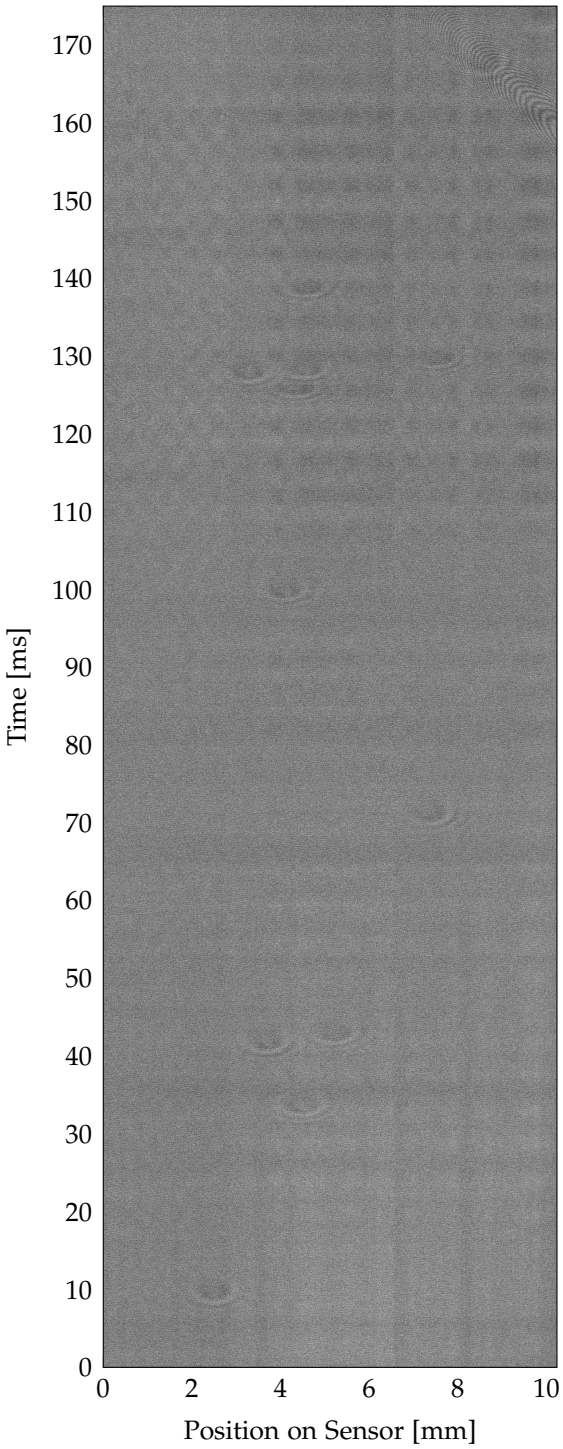

Figure B.8.: q_{MFM}=380 cm^3 min^{-1}, t_s=0.035 ms, n_I=5000, n_P=12. $\Rightarrow$ C_{calc}=11 cm^{-3}; C_{CPC} =(9 $\pm$ 10) cm^{-3}

B.2. Images recorded with the direct-beam optics

All images were recorded with the direct-beam optics as described in section 3.1. No reference CPC was available during these measurements, thus no reference concentration is stated. For high concentration images the number of visible particles was estimated by counting the particles in a fraction of the image (i.e. 100 lines).

The hologram reconstructions were calculated with *cwo_reconstruct* as is described in section 3.3.3.

Figure B.9 shows a slow but relatively big ambient dust particle which does not originate from the CNM. It is also visible that the pattern is bent to the left, this means that the horizontal speed changed during the acquisition of the image.

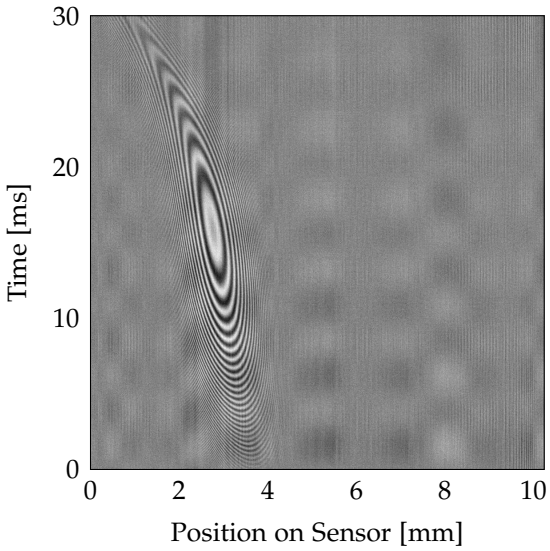

Figure B.9.: HEPA-filtered air. A very slow ambient dust particle is visible. q_{MFM}=410 cm^3 min^{-1}, t_s=0.03 ms, n_l=1000.

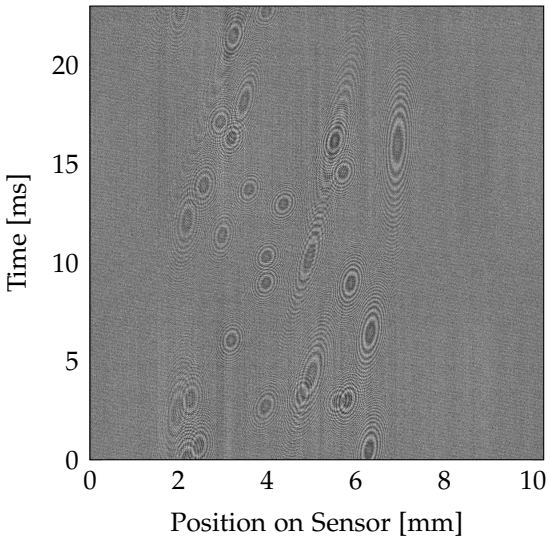

Figure B.10.: Ambient air with high dilution. q_{MFM}=595 cm^3 min^{-1}, t_s=0.023 ms, n_l=1000, n_p=32. $\Rightarrow$ C_{calc}=140 cm^{-3}.

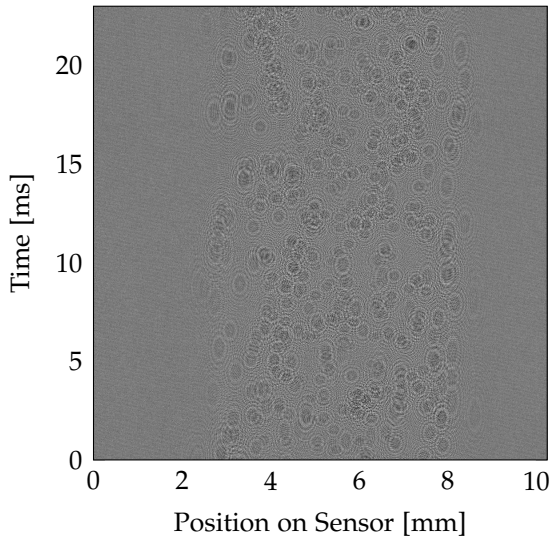

Figure B.11.: Ambient air with low dilution. q_{MFM}=860 cm^3 min^{-1}, t_s=0.023 ms, n_l=1000, n_P=270. ⇒ C_{calc}=820 cm^{-3}.

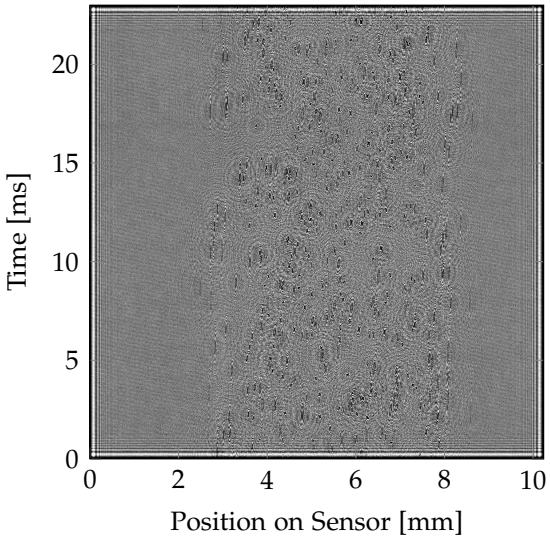

Figure B.12.: Hologram reconstruction of figure B.11 with ASM, 23 mm before the sensor plane.

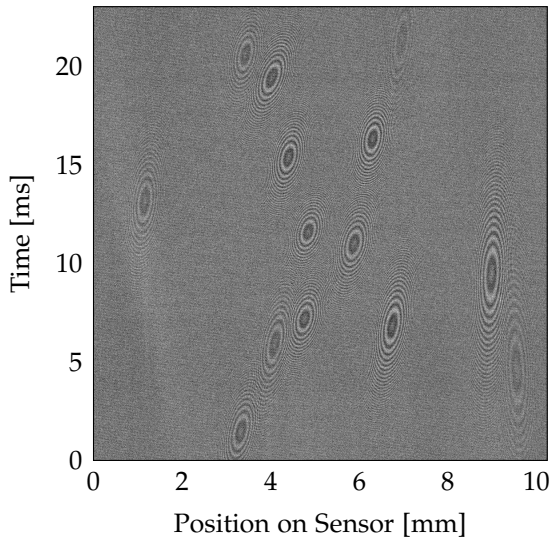

Figure B.13.: Ambient air with high dilution. q_{MFM}=500 cm^3 min^{-1}, t_s=0.023 ms, n_l=1000, n_P=14. ⇒ C_{calc}=73 cm^{-3}.

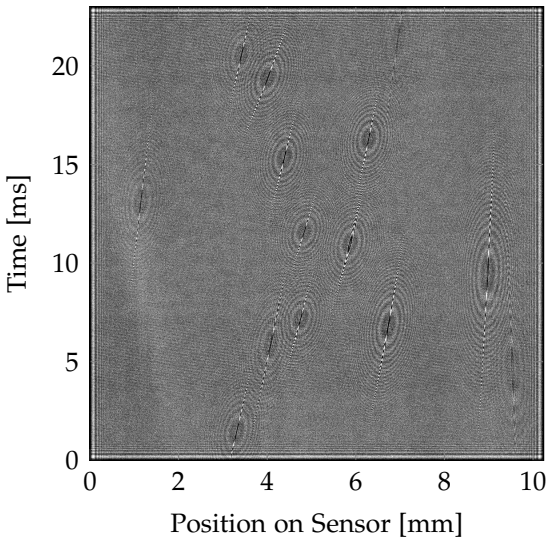

Figure B.14.: Hologram reconstruction of figure B.13 with ASM, 21 mm before the sensor plane.

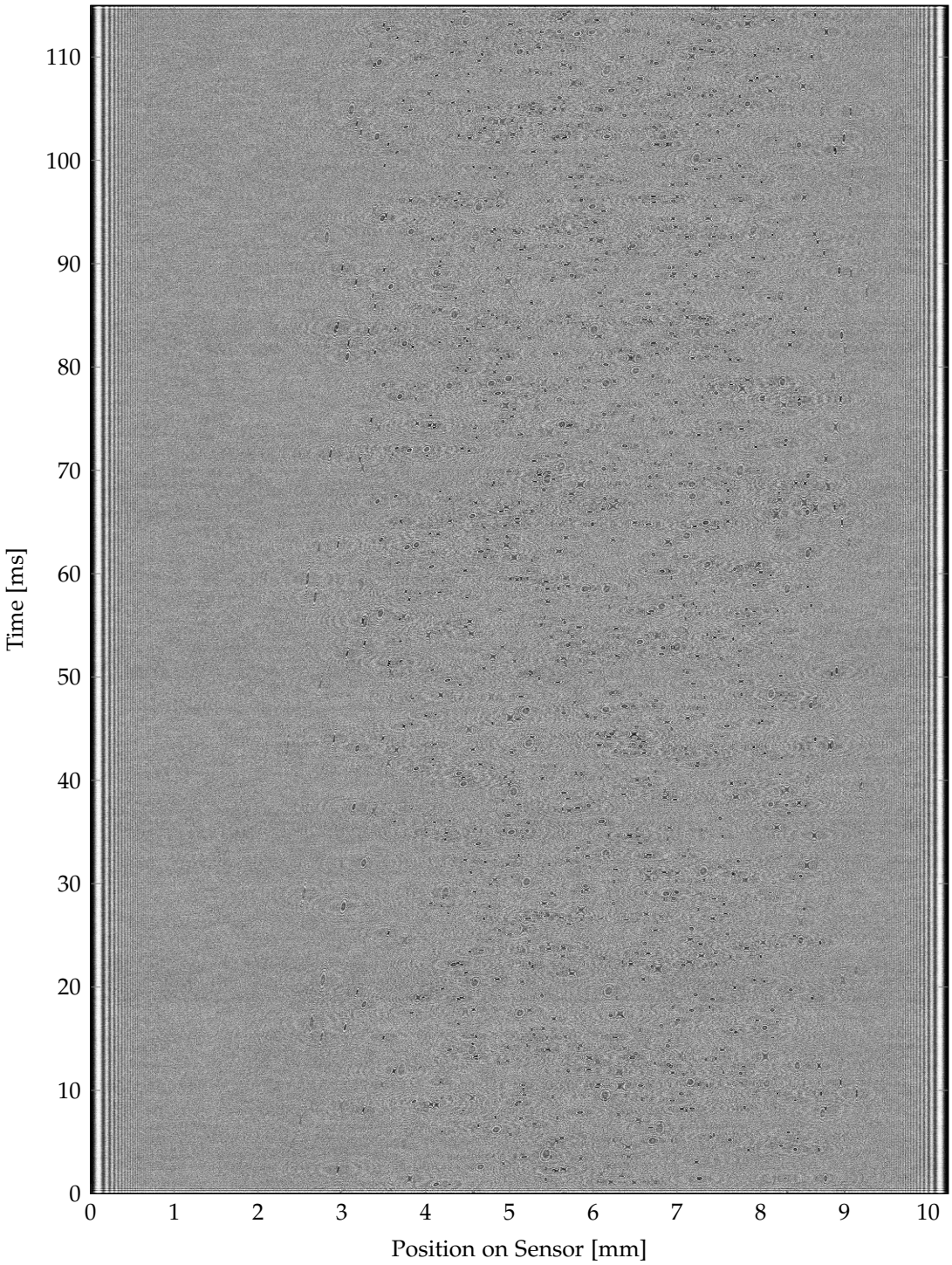

Figure B.15.: Hologram reconstruction with ASM, 23 mm before the sensor plane. The initial image was recorded with ambient air at low dilution over 115 ms. q_{MFM}=930 cm^3 min^{-1}, t_s=0.023 ms, n_L=5000, n_P=1200. $\Rightarrow$ C_{calc}=670 cm^{-3}.

Appendix C.

Program Source Codes

C.1. cam_usb

Listing C.1: C++ program *cam_usb* for image acquisition.

```
#include "stdafx.h"
#include "iostream"
#include "fstream"
#include "Sk91usb3.h"
#include "string"
#include "sstream"
#include "Windows.h"

#define CAM_ID 0
#define N_INIT_RETRY 5
#define INIT_DELAY 200

using namespace std;

int initusb()
{
  for (int i = 0; i < N_INIT_RETRY; i++)
  {
    if (SK_INITUSB() == SK_RESULT_OK) break;
    else
    {
      Sleep(INIT_DELAY);
      if (i >= N_INIT_RETRY - 1) return false;
    }
  }
  Sleep(INIT_DELAY);
  return true;
}

int initusbcam()
{
  for (int i = 0; i < N_INIT_RETRY; i++)
  {
    if (SK_INITUSBCAMERA(CAM_ID) == SK_RESULT_OK) break;
    else
    {
      initusb();
      if (i >= N_INIT_RETRY - 1) return false;
    }
  }
  return true;
}

```

```
int init_camera(int bitdepth, float int_time,float line_freq)
{
  if (initusb() == false) return false;
  if (initusbcam() == false) return false;

  SK_SETBITDEPTH(CAM_ID, bitdepth);
  SK_SETINTEGRATIONTIME(CAM_ID, int_time);

  return true;
}

int get_camerainfo(int *pixelsperline, int *imagesize, int n_lines, bool show_info)
{
  *pixelsperline = SK_GETPIXELSPERLINE(CAM_ID);
  *imagesize = *pixelsperline * SK_GETBYTESPERPIXEL(CAM_ID) * n_lines;

  if (SK_GETUSBVERSION(CAM_ID, NULL, 0) != 3)
    cout << "No USB 3.0 Connection!";

  if (show_info)
  {
    cout << "USB Version: " << SK_GETUSBVERSION(CAM_ID, NULL, 0) << endl;
    cout << "Number of lines in Buffer: " << SK_GETLINES(CAM_ID, 0) << endl;
    cout << "Set integration time: " << SK_GETINTEGRATIONTIME(CAM_ID) << " ms" << endl;
    cout << "Set frequency : " << SK_GETLINEFREQUENCY(CAM_ID) << " kHz" << endl;
    cout << "Min exposure: " << SK_GETMINEXPOSURETIME(CAM_ID) << "; Max exposure: " << SK_GETMAXEXPOSURETIME(
        CAM_ID) << endl;
    cout << "Imagesize: " << *imagesize << " byte" << endl;
  }
  cout << "Set integration time: " << SK_GETINTEGRATIONTIME(CAM_ID) << " ms" << endl;

  return true;
}

int close_camera()
{
  SK_CLOSEUSBCAMERA(CAM_ID);
  SK_CLOSEUSB();
  return true;
}

int savetofile_fprint(unsigned char cam_data[], char filename[], int bitperpixel, int pixelsperline, int
    imagesize, double *pixsum, bool messages)
{
  int i;
  FILE *camdatafile=fopen(filename,"w");
  if (messages)
    cout << "Reading from camera done. Saving File..." << endl;

  switch (bitperpixel)
  {
  case 8:
    for (i = 0; i < imagesize; i++)
    {
      *pixsum += (int)cam_data[i];
      cam_data_file << (int)cam_data[i];
      if ((i + 1) % pixelsperline == 0)
        cam_data_file << "\n\r";
      else
        cam_data_file << ";";
    }
    *pixsum /= i;

  case 12:
    for (i = 0; i < imagesize / 2; i++)
    {
      fprintf(camdatafile,"%d",((((int)cam_data[2 * i + 1]) << 8) | ((int)cam_data[2 * i])));
      if ((i + 1) % pixelsperline == 0)
        fprintf(camdatafile,"\n");
      else
        fprintf(camdatafile, ";");
    }
  }

  fclose(camdatafile);
  return true;

}
```

```
121 int makecamarray(unsigned char cam_data[], int cam_data_int[], int bitperpixel, int pixelsperline, int
        imagesize)
122 {
123
124   int i, j=0;
125   switch (bitperpixel)
126   {
127   case 8:
128     for (i = 0; i < imagesize; i++)
129     {
130       cam_data_int[i] = (int)cam_data[i];
131       if ((i + 1) % pixelsperline == 0)
132         j++;
133     }
134
135   case 12:
136     for (i = 0; i < imagesize / 2; i++)
137     {
138       cam_data_int[i] = ((((int)cam_data[2 * i + 1]) << 8) | ((int)cam_data[2 * i]));
139       if ((i + 1) % pixelsperline == 0)
140         j++;
141     }
142   }
143   return true;
144
145 }
146
147 int main(int argc, char* argv[], char *envp[])
148 {
149
150
151   int n_lines = 1000, pixelsperline, bitperpixel = 12, imagesize, *cam_data_int;
152   unsigned char *cam_data;
153   float integ_time, measurement_time, line_freq;
154   double pixsum = 0;
155   bool messages = true;
156   char datafilename[500] = "d:/camdata.txt";
157
158   stringstream cmdlinearg;
159
160   //Commandline options: 1.Value: Number of Lines, 2.: Integration Time, 3.: Frequency, 4.: Filename
161   if (argc>2)
162   {
163     cmdlinearg << argv[1]<<' '<<argv[2]<<' '<<argv[3];
164     cmdlinearg >> n_lines >> integ_time >> line_freq;
165     if (n_lines <= 0 || n_lines > 1000000)
166       return false;
167
168     if (integ_time <= 0 || integ_time > 1000)
169       return false;
170
171     if (line_freq <= 0 || line_freq > 80)
172       return false;
173
174     if (argc > 4)
175     {
176       cmdlinearg.clear();
177       cmdlinearg.str("");
178       cmdlinearg << argv[4];
179       cmdlinearg >> datafilename;
180     }
181
182
183   }
184   else
185   {
186     cout << "\n\r-----Linecam-TEST-----\n\n\r";
187
188     cout << "Number of lines: ";
189     cin >> n_lines;
190     cout << "Integration Time [ms]: ";
191     cin >> integ_time;
192     cout << "Frequency [kHz]: ";
193     cin >> line_freq;
194
195   }
196
197   if (integ_time < 0.010001) integ_time = 0.010001;
198
```

```
199   measurement_time = n_lines*integ_time;
200
201   if (init_camera(bitperpixel,integ_time,line_freq) == false)
202   {
203     cout << "\n\rInit error.\n\r";
204     return false;
205   }
206   if (messages)
207   {
208     cout << "Init OK\n\r";
209     cout << "Measurement time: " << measurement_time << "ms" << endl;
210   }
211
212
213   get_camerainfo(&pixelsperline,&imagesize,n_lines,messages);
214
215   //initialize image buffer
216   cam_data = new unsigned char[imagesize];
217   memset(cam_data, 0, imagesize);
218
219   cam_data_int = new int[n_lines*pixelsperline];
220   memset(cam_data_int, 0, n_lines*pixelsperline);
221
222
223   //Grab frame
224   if (SK_GRAB(CAM_ID, cam_data, n_lines, FALSE, 0, SK_FREERUN, (int)measurement_time+1000) != SK_RESULT_OK)
225     cout << "\n\rFrame grab error." << endl;
226   else
227     savetofile_fprint(cam_data, datafilename, bitperpixel, pixelsperline, imagesize, &pixsum, messages);
228
229   //Empty buffer
230   delete cam_data;
231   cam_data = NULL;
232
233
234   close_camera();
235   if (messages)
236   {
237     cout << "\n\r-----Done------------\n\n\r";
238     system("pause");
239   }
240   return 0;
241 }
```

C.2. cwo_reconstruct

Listing C.2: C++ program *cwo_reconstruct* for hologram reconstruction.

```
1  #include "stdafx.h"
2  #include <conio.h>
3  #include <stdlib.h>
4  #include <math.h>
5  #include <stdio.h>
6  #include "iostream"
7  #include "string"
8  #include "sstream"
9  #include "../../src/cwo.h"
10
11 #pragma comment(lib, "cwo.lib")
12
13 using namespace std;
14
15 #define _MAX_PATH 500
16
17 int main(int argc, char* argv[], char *envp[])
18 {
19
20   CWO c, orig;
21   c.SetThreads(8); //Number of CPU threads(Default is 1)
22   double d_start, d_stop, n_steps,lambda,pitch;
23   char datafilename[_MAX_PATH] = "pic1.bmp";
```

```
24    stringstream cmdlinearg;
25
26    char path_buffer[_MAX_PATH];
27    char drive[_MAX_DRIVE];
28    char dir[_MAX_DIR];
29    char fname[_MAX_FNAME];
30    char ext[_MAX_EXT];
31    errno_t err;
32
33    //Commandline Options: 1.: filename
34    if (argc>1)
35    {
36      cmdlinearg.clear();
37      cmdlinearg.str("");
38      cmdlinearg << argv[1];
39      cmdlinearg >> path_buffer;
40      printf("\n%s\n\n", path_buffer);
41
42      cout << "Start distance [m]:";
43      cin >> d_start;
44      cout << "End distance [m]:";
45      cin >> d_stop;
46      cout << "Number of Steps:";
47      cin >> n_steps;
48    }
49    else
50    {
51      exit(0);
52    }
53    err = _splitpath_s(path_buffer, drive, _MAX_DRIVE, dir, _MAX_DIR, fname, _MAX_FNAME, ext, _MAX_EXT);
54    if (err != 0)
55    {
56      printf("Error creating path. Error code %d.\n", err);
57      exit(1);
58    }
59
60    ////////////////////////
61    //Simple diffraction
62    ////////////////////////
63
64    if (!(d_start<1 && d_start >-1))
65    {
66      d_start = 16e-3;  //Meter
67      d_stop = 28e-3;   //Meter
68      n_steps = 10;
69    }
70
71    pitch= 10e-6; //Sensor pixel size meter
72    lambda = 635e-9;//Wavelength Laser Meter
73
74    printf("simple diffraction\n");
75    c.Load(path_buffer); //1024x1024 pixels bitmap image
76    c.SqrtReal();//Taking square root
77    c.SetWaveLength(lambda); //Wavelength Laser Meter
78    c.SetPitch(pitch, pitch); //Sensor Pitch Meter
79
80    orig = c;
81
82    for (int i = 0; i < n_steps; i++)
83    {
84      float dist;
85      char filen[_MAX_FNAME];
86
87      c = orig;
88      dist = (float)(d_start + i*(d_stop-d_start)/(n_steps-1)); //distance in meter
89
90      c.Diffract(dist, CWO_ANGULAR);
91      c.Intensity();  //calculating Intensity
92
93      sprintf_s(filen, "%s_diffraction_result_%f", fname,dist);
94      err = _makepath_s(path_buffer, _MAX_PATH, drive, dir, filen,ext);
95      printf("%s\n", path_buffer);
96      c.SaveAsImage(path_buffer, CWO_SAVE_AS_RE);//save diffracted intensity pattern as 256 gray scale bitmap
            file
97
98    }
99    return 0;
100 }
```

Bibliography

[1] P.A. Baron and K. Willeke. *Aerosol measurement: principles, techniques, and applications*. A Wiley-Interscience publication. Wiley, 2001. ISBN: 9780471356363. URL: http://books.google.at/books?id=nBpSAAAAMAAJ (cit. on pp. 4, 6, 17, 18).

[2] Matthew J. Berg and Gorden Videen. "Digital holographic imaging of aerosol particles in flight." In: *Journal of Quantitative Spectroscopy and Radiative Transfer* 112.11 (2011), pp. 1776–1783. ISSN: 0022-4073. DOI: http://dx.doi.org/10.1016/j.jqsrt.2011.01.013 (cit. on p. 28).

[3] Alexander Bergmann, Otto Glatter, and Gerhard Fritz-Popovski. *Kleinwinkelstreung 1*. Lecture Notes. 1997 (cit. on p. 49).

[4] Gintautas Buzorius. "Cut-Off Sizes and Time Constants of the CPC TSI 3010 Operating at 1-3 lpm Flow Rates." In: *Aerosol Science and Technology* 35.1 (2001), pp. 577–585. DOI: 10.1080/02786820121505 (cit. on p. 6).

[5] Florian Charrière, Nicolas Pavillon, Tristan Colomb, Christian Depeursinge, Thierry J. Heger, Edward A. D. Mitchell, Pierre Marquet, and Benjamin Rappaz. "Living specimen tomography by digital holographic microscopy: morphometry of testate amoeba." In: *Opt. Express* 14.16 (Aug. 2006), pp. 7005–7013. DOI: 10.1364/OE.14.007005 (cit. on p. 28).

[6] Red Pitaya d.o.o. *Red Pitaya User Manual*. Jan. 8, 2015. URL: http://wiki.redpitaya.com/index.php?title=User_Manual (visited on 01/08/2015) (cit. on p. 54).

[7] United Nations Economic Commission for Europe (UNECE). *UN Addendum 82: Regulation No. 83*. 2011. URL: http://www.unece.org/fileadmin/DAM/trans/main/wp29/wp29regs/r083r4e.pdf (cit. on pp. 1, 6, 7).

[8] Patrick Falk. "A visual-based particle counter: simulation and design." Mastersthesis. Graz University of Technology, Austria, June 2014 (cit. on pp. 8, 9, 62).

[9] Hermann Fromme. *Particles in the Indoor Environment, Air Quality - Monitoring and Modeling*. Ed. by Dr. Sunil Kumar. 2012. ISBN: 9789535101611. DOI: 10.5772/34319 (cit. on p. 11).

[10] Jacob P. Fugal, Raymond A. Shaw, Ewe Wei Saw, and Aleksandr V. Sergeyev. "Airborne digital holographic system for cloud particle measurements." In: *Appl. Opt.* 43.32 (Nov. 2004), pp. 5987–5995. DOI: 10.1364/AO.43.005987 (cit. on p. 28).

[11] Jerome Fung. "Measuring the 3D Dynamics of Multiple Colloidal Particles with Digital Holographic Microscopy." PhD thesis. Harvard University, 2013. URL: http://dash.harvard.edu/bitstream/handle/1/11181215/Fung_gsas.harvard_0084L_11200.pdf (cit. on p. 36).

[12] Jerome Fung, K. Eric Martin, Rebecca W. Perry, David M. Kaz, Ryan McGorty, and Vinothan N. Manoharan. "Measuring translational, rotational, and vibrational dynamics in colloids with digital holographic microscopy." In: *Opt. Express* 19.9 (Apr. 2011), pp. 8051–8065. DOI: 10.1364/OE.19.008051 (cit. on p. 28).

[13] Dennis Gabor. "A New Microscopic Principle." In: *Nature* 161 (1948), pp. 777–778. DOI: 10.1038/161777a0 (cit. on p. 26).

[14] Barouch Giechaskiel, Martin Cresnoverh, Herwig Joergl, and Alexander Bergmann. "Calibration and accuracy of a particle number measurement system." In: *Measurement Science and Technology* 21.4 (2010), p. 045102. DOI: 10.1088/0957-0233/21/4/045102 (cit. on pp. 2, 3).

[15] Barouch Giechaskiel, Athanasios Mamakos, Jon Andersson, Panagiota Dilara, Giorgio Martini, Wolfgang Schindler, and Alexander Bergmann. "Measurement of Automotive Nonvolatile Particle Number Emissions within the European Legislative Framework: A Review." In: *Aerosol Science and Technology* 46.7 (2012), pp. 719–749. DOI: 10.1080/02786826.2012.661103 (cit. on p. 2).

[16] Schäfter+Kirchhoff GmbH. *Laser line, Micro focus, Laser Pattern Generators*, p. 66. URL: http://www.sukhamburg.com/download/llg-kat_e.pdf (visited on 01/07/2015) (cit. on p. 13).

[17] Schäfter+Kirchhoff GmbH. *SK1024U3PD Monochrome Line Scan Camera*. URL: http://www.sukhamburg.com/download/SK1024U3PD-E-web.pdf (visited on 01/07/2015) (cit. on p. 14).

[18] J.W. Goodman. *Introduction to Fourier Optics*. McGraw-Hill Series in Electrical and Computer Engineering: Communications and Signal Processing. McGraw-Hill, 1996. ISBN: 9780070242548. URL: http://books.google.at/books?id=QllRAAAAMAAJ (cit. on pp. 26, 29).

[19] Duane Hanselman. *Fit Polynomial to Data with Constraints*. Nov. 6, 2012. URL: http://www.mathworks.com/matlabcentral/fileexchange/38926-fit-polynomial-to-data-with-constraints/content/mmpolyfit.m (visited on 01/07/2015) (cit. on p. 44).

[20] Susanne V. Hering, Mark R. Stolzenburg, Frederick R. Quant, Derek R. Oberreit, and Patricia B. Keady. "A Laminar-Flow, Water-Based Condensation Particle Counter (WCPC)." In: *Aerosol Science and Technology* 39.7 (2005), pp. 659–672. DOI: 10.1080/02786820500182123 (cit. on p. 7).

[21] Thorlabs Inc. *APD120 Series Operation Manual*. Nov. 14, 2013. URL: http://www.thorlabs.de/thorcat/MTN/APD120A2-Manual.pdf (visited on 01/08/2015) (cit. on p. 52).

[22] Thorlabs Inc. *S2011 Adjustable Focus Laser Diode Kit*. Aug. 29, 2011. URL: https://www.thorlabs.com/thorcat/5400/S2011-Manual.pdf (visited on 01/08/2015) (cit. on p. 52).

[23] TSI Inc. *Engine Exhaust Condensation Particle Counter Model 3790A*. URL: http://www.tsi.com/uploadedFiles/_Site_Root/Products/Literature/Spec_Sheets/3790_5001116_A4.pdf (visited on 01/07/2015) (cit. on p. 15).

[24] TSI Inc. *General Purpose Thermal Mass Flowmeter Model 4140/4143*. Sept. 2013. URL: http://www.tsi.com/uploadedFiles/_Site_Root/Products/Literature/Manuals/4140-4143-1980383D.pdf (visited on 01/07/2015) (cit. on p. 12).

[25] ISO. *Aerosol particle number concentration — Calibration of condensation particle counters*. ISO 27891. Geneva, Switzerland: International Organization for Standardization, 2014. URL: http://www.iso.org/iso/catalogue_detail.htm?csnumber=44414 (cit. on p. 7).

[26] J.M. *How to get the limits of rotated ellipse?* URL: http://math.stackexchange.com/questions/91132/how-to-get-the-limits-of-rotated-ellipse (visited on 01/04/2015) (cit. on p. 37).

[27] Bhaskar Jyoti Krishnatreya, Arielle Colen-Landy, Paige Hasebe, Breanna A. Bell, Jasmine R. Jones, Anderson Sunda-Meya, and David G. Grier. "Measuring Boltzmann's constant through holographic video microscopy of a single colloidal sphere." In: *American Journal of Physics* 82.1 (2014), pp. 23–31. DOI: http://dx.doi.org/10.1119/1.4827275 (cit. on p. 28).

[28] D.R. Lide. *CRC Handbook of Chemistry and Physics, 81st Edition*. CRC Handbook of Chemistry and Physics. Taylor & Francis, 2000. ISBN: 9780849304811. URL: http://books.google.at/books?id=DLKLMgEACAAJ (cit. on p. 17).

[29] K. Lüders and Gebhard von Oppen. *Klassische Physik: Mechanik und Wärme*. Bergmann/Schaefer Physik Kompakt. De Gruyter, 2012. ISBN: 9783110226676. DOI: 10.1515/9783110226683 (cit. on p. 12).

[30] Christopher Mann, Lingfeng Yu, and Myung Kim. "Movies of cellular and sub-cellular motion by digital holographic microscopy." In: *BioMedical Engineering OnLine* 5.1 (2006), p. 21. ISSN: 1475-925X. DOI: 10.1186/1475-925X-5-21 (cit. on p. 28).

[31] Octave community. *GNU Octave 3.8.2*. 2014. URL: www.gnu.org/software/octave/ (cit. on p. 17).

[32] Lars Øgendal. *Light Scattering Demystified - Theory and Practice*. July 16, 2013. URL: http://igm.fys.ku.dk/~lho/personal/lho/lightscattering_theory_and_practice.pdf (visited on 01/08/2015) (cit. on pp. 48, 49).

[33] W.S. Rasband. *ImageJ*. U. S. National Institutes of Health, Bethesda, Maryland, USA. 1997-2014. URL: http://imagej.nih.gov/ij/ (cit. on p. 33).

[34] T. Shimobaba, J. Weng, T. Sakurai, N. Okada, T. Nishitsuji, N. Takada, A. Shiraki, N. Masuda, and T. Ito. "Computational wave optics library for C++: CWO++ library." In: *Computer Physics Communications* 183 (May 2012), pp. 1124–1138. DOI: 10.1016/j.cpc.2011.12.027 (cit. on pp. 28, 30).

[35] Tomoyoshi Shimobaba, Hiroya Yamanashi, Takashi Kakue, Minoru Oikawa, Naohisa Okada, Yutaka Endo, Ryuji Hirayama, Nobuyuki Masuda, and Tomoyoshi Ito. "In-line digital holographic microscopy using a consumer scanner." In: *Scientific Reports* 3 (Sept. 16, 2013). DOI: 10.1038/srep02664 (cit. on p. 28).

[36] Herbert Sigloch. *Technische Fluidmechanik*. Springer London, Limited, 2007. ISBN: 9783540446354. URL: http://books.google.at/books?id=8rWvskmYvs4C (cit. on pp. 18, 44).